



# Diagnosing the shape parameters of the gamma particle size distributions in a two-moment microphysics scheme and improvements to explicit hail prediction

Liping Luo<sup>a,\*,\*\*</sup>, Ming Xue<sup>b,c,\*</sup>, Kefeng Zhu<sup>d</sup>, Zhaomin Wang<sup>a</sup>

<sup>a</sup> College of Oceanography, Hohai University, Nanjing 210098, China

<sup>b</sup> Key Laboratory of Mesoscale Severe Weather/Ministry of Education and School of Atmospheric Sciences, Nanjing University, Nanjing 210093, China

<sup>c</sup> Center for Analysis and Prediction of Storms and School of Meteorology, University of Oklahoma, Norman, OK 73072, USA

<sup>d</sup> CMA Key Laboratory of Transportation Meteorology, Nanjing Joint Institute for Atmospheric Sciences, Nanjing 210041, China

## ARTICLE INFO

### Keywords:

Multi-moment microphysics scheme  
Diagnostic shape parameter  
Numerical simulation  
Explicit hail prediction

## ABSTRACT

Three-moment bulk microphysics schemes are attractive since they can determine the shape parameter  $\alpha$  of the gamma particle size distributions (PSDs) from the predicted moments, but they are more computationally expensive compared with two-moment schemes. In this study, new diagnostic relations between  $\alpha$  and the mean-mass diameter are developed for rain, graupel and hail hydrometeor categories based on the simulations for a severe hailstorm over eastern China using the Milbrandt and Yau (MY) three-moment scheme.

The new relations are introduced into the MY two-moment scheme and applied to the simulation of the same hailstorm at 1 km grid spacing. Different configurations of the MY schemes, including one-moment, two-moment with fixed  $\alpha$ , with the original and new  $\alpha$  diagnostic relations, and with the new  $\alpha$  relation applied to hail only, and three-moment schemes, are also used to simulate the hailstorm. The new fully diagnostic- $\alpha$  two-moment scheme is found to improve the simulation of the general storm structure compared with the other two-moment schemes. It also reproduces the maximum estimated size of hail closer to that from the three-moment scheme while still retaining computational efficiency. Explicit prediction of hail by the new diagnostic- $\alpha$  two-moment scheme, including the surface accumulated hail mass, number and distribution is the most consistent with that of the three-moment scheme. The experiment with the new  $\alpha$  relation applied to hail only predicts a larger number of smaller hail and higher radar reflectivity, consistent with rain and graupel size over-estimation from excessive size sorting. Detailed microphysical budget analyses for hail, graupel and rain indicate that the new diagnostic relations yield substantial improvements in hydrometeor mass growth processes and size sorting representation.

## 1. Introduction

With the continuous increase in computing power and model resolution, microphysics parameterization (MP) becomes increasingly essential for numerical weather prediction. The MP schemes parameterize the formation of cloud and hydrometeor particles, their growth and interactions, and their fallout as precipitation. However, a number of studies (e.g., Hong et al., 2004; Milbrandt and Yau, 2006a, 2006b, hereafter MY06a, b; Morrison et al., 2009; Jung et al., 2010; Dawson et al., 2010, 2015; Putnam et al., 2014, 2017; Planche et al., 2019; Labriola et al., 2019a, 2019b; Morrison et al., 2020; Wang et al., 2020)

have shown that parameterization of microphysical processes is a substantial source of uncertainty within convective scale forecasts.

According to the representation of cloud and precipitation particle size distributions, MP schemes can be broadly characterized as spectral bin, bulk, and Lagrangian particle-based schemes. Bin schemes (e.g., Khain and Pokrovsky, 2004; Lynn et al., 2005a, 2005b) generally predict the evolution of the particle size distributions (PSDs) by discretizing the PSDs across tens of size or mass bins, which allow more flexible PSDs. Bulk schemes (e.g., Milbrandt and Yau, 2005a, 2005b, hereafter MY05a, b; Hong et al., 2006; Thompson et al., 2008; Morrison et al., 2009; Mansell, 2010) typically assume certain functional forms of PSDs and

\* Corresponding author at: CAPS, University of Oklahoma, Norman, Oklahoma 73072, USA.

\*\* Corresponding author at: College of Oceanography, Hohai University, Nanjing 210098, China.

E-mail addresses: [lpingluo@hhu.edu.cn](mailto:lpingluo@hhu.edu.cn) (L. Luo), [mxue@ou.edu](mailto:mxue@ou.edu) (M. Xue).

predict specific moments of the PSDs so as to determine the free parameters within. In Lagrangian particle-based schemes, the PSD (e.g., Andrejczuk et al., 2010; Riechelmann et al., 2012; Brdar and Seifert, 2018) is represented by sampled “super-particles” with multiplicity factor, providing a path towards numerical convergence for cloud modelling in principle. However, as bin and Lagrangian particle-based schemes are much more expensive computationally, costing at least an order of magnitude more than bulk schemes, bulk schemes are the workhorses in operational weather prediction and related research (e.g., Morrison and Pinto, 2005; MY06a, b; Loftus et al., 2014; Loftus and Cotton, 2014; Pan et al., 2016; Labriola et al., 2017, 2019a, 2019b; Luo et al., 2017, 2018, 2020, L17, L18 and L20 hereafter respectively; Johnson et al., 2019; Zhu et al., 2018; Zhu et al., 2020). Besides, recent studies have highlighted large uncertainties in ice microphysics and numerical diffusion processes across mass bins in bin schemes, which can result in large spread across simulations (vanZanten et al., 2011; Xue et al., 2017; Grabowski et al., 2019). With the particle-based schemes, Grabowski et al. (2019) noted significant uncertainties in the initialization of super-particles while more efficient treatment of collisional breakup processes for particle-based schemes is numerical challenging (Morrison et al., 2020).

The PSDs in bulk MP schemes directly impact microphysical processes of all categories and terminal velocities of hydrometeors. The three-parameter Gamma distribution is the most widely used form of PSD (e.g., MY05a, b; Morrison et al., 2009; Mansell, 2010), as given by equation

$$N(D) = N_0 D^\alpha \exp(-\lambda D) \quad (1)$$

where  $N_0$ ,  $\alpha$  and  $\lambda$  are often referred to as the intercept, shape and slope parameters, respectively, while  $D$  is the diameter of the particle. The simplest bulk schemes predict only one moment of PSD for each hydrometeor — usually the third moment or hydrometeor mass mixing ratio ( $Q$ ) while specifying  $N_0$  and  $\alpha$  as fixed values (e.g., Kessler, 1969; Hong et al., 2006; Lin and Colle, 2011; Bae et al., 2019). In two-moment schemes,  $Q$  and the total number concentration ( $N_T$ ) of the hydrometeors are predicted (e.g., MY05a; Thompson et al., 2008; Morrison et al., 2009; Mansell, 2010; Bae et al., 2016; Lei et al., 2020). Thus,  $\lambda$  and  $N_0$  can be diagnosed based on  $Q$  and  $N_T$  when  $\alpha$  is prescribed as a constant value. More recently, another type of two-moment microphysics scheme predicting bulk particle properties (P3) for single ice category has been developed (Morrison and Milbrandt, 2015), which provides a new approach to the representation of ice particle evolution. Milbrandt and Morrison (2016) expanded the P3 scheme to include multiple ice categories by allowing ice particles with different bulk properties to coexist. However, several studies have noted that the P3 scheme is problematic in predicting the hail distribution within a storm (Labriola et al., 2019b) and cannot generate the polarimetric signatures identified in the observations (Johnson et al., 2019). To further improve the P3 schemes, Milbrandt et al. (2021) proposed a three-moment representation of the size distribution of ice categories; results from sensitivity simulations suggest that the new three-moment ice version of P3 scheme can better handle gravitational size sorting of ice and improve the representation of heavily rimed ice. They also noted that three-moment representation of rain (Paukert et al., 2019) and better parameterization of ice melting (Cholette et al., 2019) might also help to address the underestimation of radar reflectivity in the three-moment P3 scheme.

To obtain a fully prognostic gamma PSD for each category, three-moment schemes were developed (e.g., MY05b; Loftus et al., 2014), which predict  $Q$ ,  $N_T$  and the sixth-moment radar reflectivity factors ( $Z$ ) of the hydrometeors. Comparisons against observations suggested that the simulated storm propagation, storm structure and microphysical fields were better reproduced by simulations using three-moment schemes than using one- or two-moment schemes (e.g., MY06b; Loftus and Cotton, 2014; Dawson et al., 2015; L17, L18). Nevertheless, as an additional variable (i.e.,  $Z$ ) associated with each species needs to be

predicted, three-moment schemes are computationally more expensive than corresponding two-moment schemes. Moreover, due to the independent variations of the total number concentrations of hydrometeors in two-moment schemes and the allowance for size sorting, dramatic improvements can be achieved in simulated storm structures and precipitation fields when changing from one to two-moment schemes (MY06b; Dawson et al., 2010). Thus, two-moment schemes have become more widely used in recent years (e.g., Mansell et al., 2010; Grabowski and Morrison, 2016; Snook et al., 2016; Xu et al., 2017; Zhu et al., 2018; Zhu et al., 2020; Planche et al., 2019; Wang et al., 2020).

However, several studies have concluded that two-moment schemes with fixed values for  $\alpha$  often suffer from excessive size sorting; and the size sorting rate increases as  $\alpha$  decreases (e.g., MY05a; Milbrandt and McTaggart-Cowan, 2010; Kumjian and Ryzhkov, 2012). Besides, Brandes et al. (2002) also found that the  $\alpha$  of raindrops observed from convective and stratiform rain in Florida and Oklahoma varies widely from  $-2$  to  $10$ . Therefore, different approaches have been proposed to curtail excessive size sorting in two-moment schemes by deriving relations of  $\alpha$  from observations and simulations using more complicated MP schemes. For example, Zhang et al. (2001) proposed a method to calculate gamma distribution parameters for rain based on radar observations, including reflectivity and differential reflectivity; a constrained-gamma distribution model with relations between  $\alpha$  and  $\lambda$  parameters was also derived from video disdrometer measurements. Besides, other relationships between  $\alpha$  and  $\lambda$  have been derived based on both radar and disdrometer observations (e.g., Zhang et al., 2006; Cao et al., 2008), but these relations are less accurate across different rain regions (Naumann and Seifert, 2016). Moreover, the relations derived from disdrometer observations at the surface are limited to rain at the low levels.

As bin schemes can generate more flexible PSDs and three-moment schemes can directly predict  $\alpha$ , they have been taken as benchmarks to derive relationships of  $\alpha$  in two-moment schemes; in particular, the empirical relations between  $\alpha$  and mean-mass diameter ( $D_m$ ) are commonly used (e.g., MY05a; Seifert, 2008; Milbrandt and McTaggart-Cowan, 2010). MY05a was the first to postulate  $\alpha$ - $D_m$  relations based on a simulation using the Milbrandt and Yau (MY) three-moment scheme applied in a one-dimensional column mode where only sedimentation processes of the hydrometeors are considered. More recently, to improve the original diagnostic relations of  $\alpha$  in the two-moment P3 scheme, new  $\alpha$ - $D_m$  relations of ice categories were derived based on an idealized supercell simulation using three-moment ice version of P3 scheme (Milbrandt et al., 2021). Earlier, Seifert (2008) and Milbrandt and McTaggart-Cowan (2010) derived different  $\alpha$ - $D_m$  relations for hydrometeors using bin schemes in one-dimensional idealized simulations. However, Naumann and Seifert (2016) noted that as the relations between  $\alpha$  and  $D_m$  were derived from idealized heavy precipitation events, they are unsuitable for shallow cumulus simulations. L18 noted that the diagnosed  $\alpha$  of hail within the original diagnostic- $\alpha$  two-moment MY scheme (MY05a) differed significantly from the values predicted by three-moment MY scheme for a hailstorm over eastern China. As an extension of the study of L18, in this study, we develop new diagnosed  $\alpha$  relations based on output from a three-moment MY scheme simulation of the hailstorm, and apply the relations to the multi-moment version of MY scheme. Few earlier studies with diagnostic- $\alpha$  schemes have focused on hailstorms, with that of MY06b being an exception.

The MY bulk schemes are selected in this study because they have been widely used for severe storm simulations (e.g., MY06a, b; Dawson et al., 2010, 2015; Wainwright et al., 2014; Pan et al., 2016; Putnam et al., 2017; L17, L18; Labriola et al., 2019a, 2019b); plus, the package contains one-, two- and three-moment options. Also, it has both graupel and hail categories, which allows it to produce more realistic storm structures and hail signatures (Johnson et al., 2019).

Specifically, the goals of this study are two-fold. Firstly, new relations between the  $\alpha$  and  $D_m$  of precipitating hydrometeors, i.e., rain, graupel, and hail, are developed, based on a real case simulation using the MY three-moment scheme at 1-km grid spacing for a severe

hailstorm event on 28 April 2015 in eastern China. Because the range of snow  $D_m$  is narrow, no appropriate  $\alpha$ - $D_m$  relation is found for snow, so  $\alpha$  for snow is set to a constant value. Secondly, the new relations are implemented into the MY two-moment scheme within the Advanced Regional Prediction System (ARPS, Xue et al., 2000, 2001, 2003), and its hail forecast skill for the same case is evaluated through comparison with radar and other observations and with simulations with different treatment of the shape parameters. Microphysical budget analyses on the source and sink terms associated with the hydrometeors are performed to understand how the shape parameters affect hail prediction.

The remainder of this paper is structured as follows. Section 2 provides a brief overview of the severe hailstorm event, and Section 3 documents the metrics used to diagnose the  $\alpha$ - $D_m$  relations of hydrometeors in the diagnostic- $\alpha$  two-moment scheme. The design of the sensitivity simulations and the model setup are described in Section 4. Section 5 evaluates the explicit hail prediction skills of the diagnostic- $\alpha$  two-moment scheme against other simulations. The reasons for the difference in performance are also investigated by examining the PSDs within the storms and performing detailed budget analyses for rain, graupel and hail categories. Finally, a summary and conclusions are presented in Section 6.

## 2. Overview of the hailstorm event

In the afternoon of 28 April 2015, a long-duration, hail-producing, multi-cellular convective system (MCS) swept southeastward through most of Jiangsu Province, China, producing a large number of egg-sized hailstones accumulated on the ground. According to the severe weather reports from the China Meteorological Administration (CMA), egg-sized hail fell over Jiangsu and lasted for nearly seven hours (from around 0700 to 1400 UTC), accompanied by intense lightning and damaging surface winds ( $>23 \text{ m s}^{-1}$ ). L20 noted that the lifecycle of this long-lasting, hail-producing MCS is characterized by two stages. In the first stage, a series of convective cells initiated along the northwest border of Jiangsu Province and the storms organized into a northwest-southeast line as they moved southeastward. In the second stage, the MCS eventually evolved into an eastward-moving bow-echo structure. The MCS produced a long swath of hailfall from northwestern through southeastern Jiangsu Province (L18).

The synoptic patterns associated with this event showed that northeastern coastal regions of China were located ahead of a deep, southeastward-tilted, upper-level East Asian trough, and underneath the corresponding East Asian upper-tropospheric jet stream (c.f., Fig. 3a in L18). From middle to lower levels, a strong convergence zone from the northwest through southeast Jiangsu Province was set up between two vortices, with one overland and one over the East China Sea (c.f., Figs. 3b–d in L18). Moreover, L20 found that an earlier MCS played critical roles in generating and enhancing the over-sea vortex via baroclinic vorticity generation at the leading edge of its rearward spreading cold pool. Moreover, sounding and wind profiler radar observations in Nanjing City Jiangsu Province, showed high convective available potential energy reaching  $2476 \text{ J kg}^{-1}$  at 0600 UTC 28 April and strong 0–6 km vertical wind shear of  $\sim 15$  to  $\sim 23 \text{ m s}^{-1}$  between 0600 and 1200 UTC 28 April (Xu et al., 2016). The sounding also presented a dry and cold layer above a warm and humid near-surface layer, which was conducive to larger hailstones reaching the ground (Costa et al., 2001; L17).

## 3. Fitting of $\alpha$ - $D_m$ relations for two-moment microphysics scheme

Shape parameter  $\alpha$  has important effects on microphysical processes. For example, increase in  $\alpha$  represents narrowing of the hydrometeor PSD that can result from microphysical processes such as size sorting (MY05a), and most microphysical processes depend on the PSD. Thus, it is crucial to obtain realistic temporal and spatial variations of  $\alpha$ .

However,  $\alpha$  is assumed as a constant in widely used two-moment MP schemes (e.g., Seifert and Beheng, 2006; Thompson et al., 2008; Morrison et al., 2009; Mansell, 2010; Lim and Hong, 2010; Morrison and Milbrandt, 2015). In the MY three-moment scheme (MY05b),  $\alpha$  can be directly computed from the predicted moments, and verifications against observations indicate that the MY three-moment scheme reproduces storm evolution and hydrometeor distributions within storms the best compared with other schemes (e.g., MY06a; Dawson et al., 2015; L18). The advantages of the MY three-moment scheme are ascribed to its more flexible treatment of PSDs compared with its one- and two-moment counterparts, and its capability to limit excessive size sorting by converging the weighted fall speeds of the hydrometeor towards the same value (Dawson et al., 2014). Here, we want to point out that in the three-moment MY scheme, rain break-up does not impact the prediction of radar reflectivity, but only indirectly impact the prediction of total number concentration with a bulk collection efficiency. Snow fragmentation or aggregation are not accounted for either. These processes would cause spectral broadening and their omission to some extent affects the ability for the three-moment MY scheme to accurately predict the shape parameters of hydrometeor DSDs. For this reason, there are limitations to our fitted relations as well. An alternative approach is try to formulate bulk two-moment microphysics scheme based on more flexible special bin model, and the recent study of Paukert et al. (2019) is an effort in this direction. The latter approach is, however, much more complex than diagnosing new shape parameters and is therefore beyond the scope of this paper.

In this study, we derive the diagnostic relations between  $\alpha$  and  $D_m$  for the MY two-moment scheme based on a simulation using the MY three-moment scheme for the severe hailstorm on 28 April 2015 over Jiangsu Province, China, with ARPS. Following MY05a, the mean-mass diameter  $D_{mx}$  (mm) for each hydrometeor is given by

$$D_{mx} = \left[ \frac{\rho Q_x}{c_x N_{Tx}} \right]^{1/3} \quad (2)$$

where  $c_x = \frac{\rho}{\rho_x}$ ,  $\rho$  and  $\rho_x$  ( $\text{kg m}^{-3}$ ) are the ambient air density and hydrometeor density of category  $x$ , respectively;  $Q_x$  is the hydrometeor mixing ratio and  $N_{Tx}$  is the total number concentration. Earlier studies (e.g., MY05a; Seifert, 2008; Milbrandt and Mctaggart-Cowan, 2010) found relations between  $\alpha$  and  $D_m$ , although the relations obtained were based on one-dimensional idealized simulations. Thus, this study attempts to obtain more general and realistic relations of  $\alpha$  based on a real hailstorm simulation using the MY three-moment scheme. Our previous study (L18) successfully reproduced the hailstorm evolution, storm structure and intensity using this three-moment scheme. In particular, the hail prediction skill of the three-moment scheme was found to be better than the one- or two-moment MY schemes. Thus, the output data of three-moment simulation at 1-km grid spacing every ten min between 0600 and 1600 UTC 28 April 2015 covering entire Jiangsu Province are used to diagnose the relations of  $\alpha$  with  $D_m$ . As we focus on the storm regions, thresholds are applied to the predicted mixing ratio ( $Q_x$ ), total number concentration ( $N_{Tx}$ ) and radar reflectivity factor ( $Z_x$ ) for each hydrometeor ( $x$  refers to rain, snow, graupel, and hail categories) for data fitting. As  $Q_x$ ,  $N_{Tx}$  and  $Z_x$  are independently predicted in the three-moment scheme, their thresholds are independently determined as  $1 \times 10^{-5} \text{ kg kg}^{-1}$ ,  $1 \text{ m}^{-3}$  and  $1 \times 10^{-18} \text{ m}^6 \text{ m}^{-3}$  in our case, respectively.

Fig. 1 shows the scatterplots of  $\alpha$  versus  $D_m$  for each hydrometeor. The scatters reveal high variability of  $\alpha$  for the hydrometeors generated by the three-moment scheme, with the  $\alpha$  of rain, graupel and hail changing from zero to six (Figs. 1a–c), and the  $\alpha$  of snow being larger than ten (Fig. 1d). The range of prognostic  $\alpha$  for rain is generally consistent with rainfall drop size distribution observations in East China (e.g., Chen et al., 2013; Wen et al., 2017a, 2017b, 2019), which also indicate that the default constant value of  $\alpha$  in most two-moment schemes is clearly not reasonable. To obtain more general results, the  $D_m$  of each hydrometeor is divided into ten bins. Following Zhang et al.

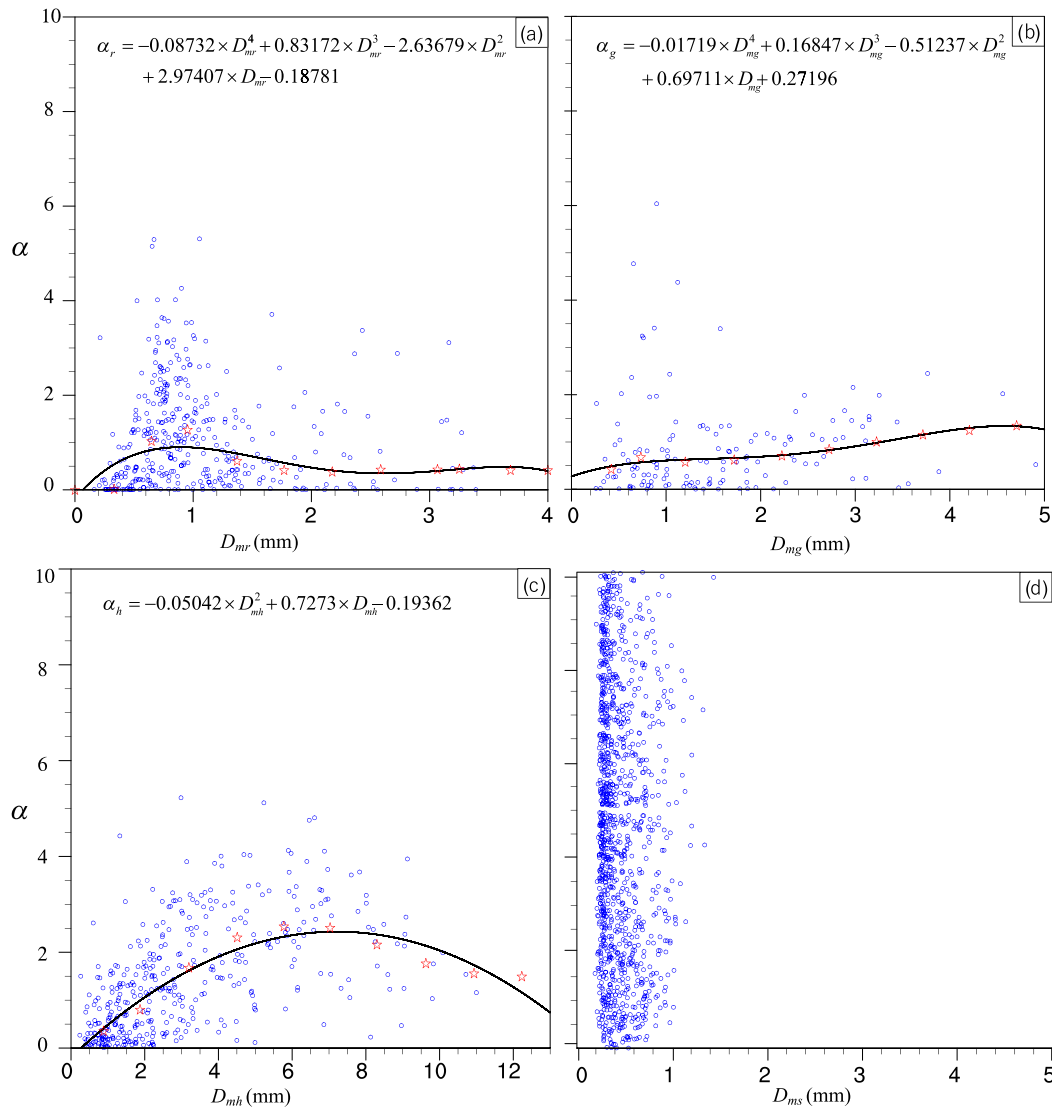


**Fig. 1.** Scatterplots and fits of shape parameter  $\alpha$  and mean-mass diameter  $D_m$  obtained from the CNTL experiment using the MY three-moment scheme for (a) rain, (b) graupel, (c) hail and (d) snow. For clarity, every five thousand points out of those used in the fitting are plotted. For the purpose of fitting, the  $D_m$  values of each hydrometeor categories are divided into ten bins and the red stars show the average pairs of  $\alpha$ - $D_m$  for each bin, and the solid black lines are the corresponding relations fitted to the stars. For snow,  $D_{ms}$  values remain within a small range between 0.25 and 1.5 mm, and there is no clear relation between its shape parameter and  $D_{ms}$  so no fit relation is derived for snow.

(2001), the least-squares polynomial fit is applied to the averaged  $\alpha$  and  $D_m$  in each bin, resulting in

$$\alpha = c_1 D_m^4 + c_2 D_m^3 + c_3 D_m^2 + c_4 D_m + c_5, \tag{3}$$

where  $c_1, c_2, c_3, c_4$  and  $c_5$  are the constants for rain, graupel and hail, summarized in Table 1. The fits on averaged  $\alpha$ - $D_m$  pairs within each bin for rain, graupel, and hail represent well the overall dependence of the two parameters (solid black lines in Figs. 1a–c). As the higher frequencies of smaller  $\alpha$  for rain, graupel and hail are applied to the fits to the averaged  $\alpha$ - $D_m$  pairs (Figs. 1a–c), there may exist somewhat low

**Table 1**  
Constants in the new diagnostic relations of  $\alpha$  for all hydrometeors.

Category $x$	$c_{1x}$	$c_{2x}$	$c_{3x}$	$c_{4x}$	$c_{5x}$
Rain	-0.08732	0.83172	-2.63679	2.97407	-0.18781
Graupel	-0.01719	0.16847	-0.51237	0.69711	0.27196
Hail	n/a	n/a	-0.05042	0.7273	-0.19362
Snow	n/a	n/a	n/a	n/a	4.6

biases in the derived  $\alpha$  due to the sampling biases of the smaller values of  $\alpha$ . Note that the snow  $D_m$  values stay within a small range of 0.5–1.0 mm (Fig. 1d) and all snow  $\alpha$  values have a similar frequency, such that no appropriate relation between snow  $\alpha$  and  $D_m$  can be found therefore the mean  $\alpha$  value of snow in the three-moment simulation, which is about 4.6, is used here. The new diagnostic  $\alpha$ - $D_m$  relations for rain, graupel and hail are then implemented into the MY two-moment scheme, and the new scheme is applied to the simulations of the same hailstorm, and another hailstorm studied in L17. The results of the latter case are not shown due to space limitation.

#### 4. Configurations of numerical experiments

Simulations of the Jiangsu hailstorm are performed using the ARPS model, and the setup of the numerical experiments is identical to that of L18. All experiments are initialized at 0000 UTC 28 April 2015 and run for 16 h. The National Centers for Environmental Prediction (NCEP) operational global model final analysis dataset at  $1^\circ \times 1^\circ$  resolution is used for the initial and boundary conditions. Two one-way nested

domains at horizontal grid spacing of 3 km and 1 km are used, and the size of the inner domain at 1-km resolution is  $460 \times 460 \text{ km}^2$ , covering almost the whole of Jiangsu Province (Fig. 2). Fifty-three vertical levels are used, with the vertical grid spacing varying from 50 m near the surface to 1000 m at the model top, stretching according to a hyperbolic tangent function. A lateral boundary relaxation zone of twelve grids is employed to allow for gradual transition of the model solution towards that of external boundary condition so as to avoid near-boundary discontinuity (Xue et al., 1995). A fourth-order monotonic computational mixing scheme (Xue et al., 2000) with a coefficient of  $0.005 \text{ s}^{-1}$  is applied to suppress numerical noise, and the subgrid-scale turbulent mixing is parameterized by a 1.5-order turbulence kinetic energy scheme. More detailed descriptions about the physics options in the ARPS model can be found in Xue et al. (2001, 2003).

To evaluate the relative performance of the new  $\alpha$ - $D_m$  relations for hydrometeors implemented into the two-moment MY scheme within ARPS, simulation experiments are performed using one-, two-, and three-moment options of the MY schemes. The experiment using the three-moment scheme is taken as the benchmark and is called the CNTL experiment. There are four two-moment experiments, named FixA, DiagA, DiagA\_NewFit and DiagA\_HailFit. FixA uses a fixed  $\alpha$  of zero for all the categories, DiagA uses the default  $\alpha$ - $D_m$  relations proposed by MY05a; DiagA\_NewFit uses the new  $\alpha$ - $D_m$  relations derived for all hydrometeors within this study, and DiagA\_HailFit uses the new  $\alpha$ - $D_m$  relation for hail only while setting  $\alpha$  for rain and graupel to fix zero value. Through comparison with FixA, experiments DiagA\_HailFit and DiagA\_NewFit are designed to investigate how much difference the newly derived relations for hail alone and for all hydrometeors make to hail prediction. The simulation using the one-moment MY scheme is named Single, with  $\alpha$  and  $N_0$  for all categories taking on default constant values. Key parameters of all experiments are summarized in Table 2.

## 5. Results

The results of simulations and hail prediction skills using different MP schemes are presented and discussed in this section. Diagnostics on the microphysical processes are also performed to help understand how the shape parameter  $\alpha$  affects hail prediction.

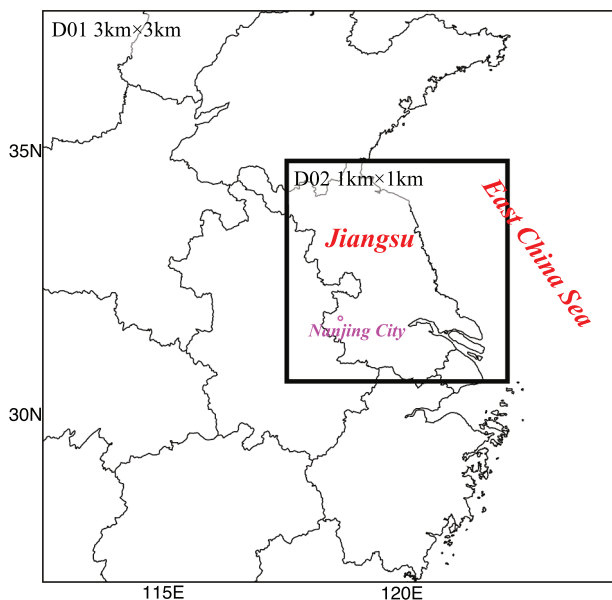


Fig. 2. Model domains at 3- and 1-km (outer and inner boxes) grid spacings for simulation experiments.

Table 2

List of sensitivity simulations using a package of MY schemes.

Experiment	Description
CNTL	Three-moment scheme, three parameters of PSD prognostic
FixA	Two-moment scheme, fixed $\alpha$ of zero for $x \in$ (ice, rain, snow, graupel, and hail)
DiagA	Two-moment scheme, diagnostic $\alpha$ based on relations proposed by MY05a for $x$
DiagA_NewFit	Two-moment scheme, diagnosed $\alpha$ based on new relations for rain, graupel and hail; for ice, $\alpha = 0$ ; for snow, $\alpha = 4.6$
DiagA_HailFit	Same as in DiagA_NewFit, but fixed $\alpha = 0$ for rain and graupel
Single	One-moment scheme, fixed $\alpha = 0$ for $x$ $N_{Tcloud} = 1 \times 10^8 \text{ m}^{-3}$ ; $N_{Orain} = 8 \times 10^6 \text{ m}^{-4}$ ; $N_{Osnow} = 3 \times 10^6 \text{ m}^{-4}$ ; $N_{Ograupel} = 4 \times 10^5 \text{ m}^{-4}$ ; $N_{Ohail} = 4 \times 10^4 \text{ m}^{-4}$

### 5.1. Comparison of simulated reflectivity to radar observations

Compared with radar observations, all experiments generally capture the overall structure and evolution of the hailstorm system, albeit there still exist differences between observations and simulations when comparing the convective cells on the one to one basis (not shown). For example, Fig. 3 shows the composite (column-maximum) radar reflectivity fields of the hailstorm system at 1100 UTC 28 April 2015 from radar observations and the six experiments using the one-, two- and three-moment configurations of the MY microphysics. It is clear that peak values of radar reflectivity lower than 60 dBZ in Single and DiagA at 1100 UTC are underestimated (Figs. 3b, d), while FixA overestimates the hailstorm intensity, predicting larger areas of high reflectivity (>60 dBZ) (Fig. 3c). The reasons for the differences in storm intensities among the experiments have been presented in L18.

The radar reflectivity fields predicted by DiagA\_NewFit resembles that of CNTL more than DiagA\_HailFit does (Figs. 3 e, f, g), as DiagA\_HailFit slightly overestimates reflectivity compared to CNTL, especially over areas of stratiform clouds (Figs. 3f, g). The reflectivity differences between FixA, DiagA\_HailFit and DiagA\_NewFit are due to their different treatments of  $\alpha$  for rain, graupel, and hail. FixA uses fixed  $\alpha$  of zero for all categories, DiagA\_HailFit only applies the new relation for hail with  $\alpha$  for rain and graupel being set to zero, while DiagA\_NewFit uses the new  $\alpha$  relations for rain, graupel, and hail. More discussions on the impacts of the newly derived  $\alpha$  relations applied to hail alone and to all three hydrometeor categories will be presented later. In short, the experiment using a two-moment scheme with the new  $\alpha$ - $D_m$  relations diagnosed from output of a three-moment simulation produces simulated reflectivity that is close to that of the three-moment experiment, but at a lower cost. Here, we point out that given many uncertainties with the reflectivity calculations from the predicted microphysical states (e.g., the wetness of hail), the comparison of simulated reflectivity against observations should be viewed with some caution.

### 5.2. Hail prediction skills using different MP schemes

To further evaluate the impacts of the new  $\alpha$ - $D_m$  relations on hail prediction, the predicted maximum estimated size of hail (MESH; Witt et al., 1998), surface accumulated hail number concentration (SAHNC; L18), and surface accumulated hail mass (SAHM) from all experiments are examined.

#### 5.2.1. MESH

The MESH algorithm has been widely used in both operational forecasting and research studies to estimate the maximum hail size arriving at the surface (e.g., Witt et al., 1998; Cintineo et al., 2012; Snook et al., 2016; Labriola et al., 2017; L17, L18). The main attractive aspect of MESH is its relatively uniform spatial coverage; it is much less sensitive to population bias as surface-based hail reports are (e.g., Wyatt and Witt, 1997; Davis and LaDue, 2004; Snook et al., 2016). In short, MESH (Witt et al., 1998) estimates the maximum size of hail occurring at

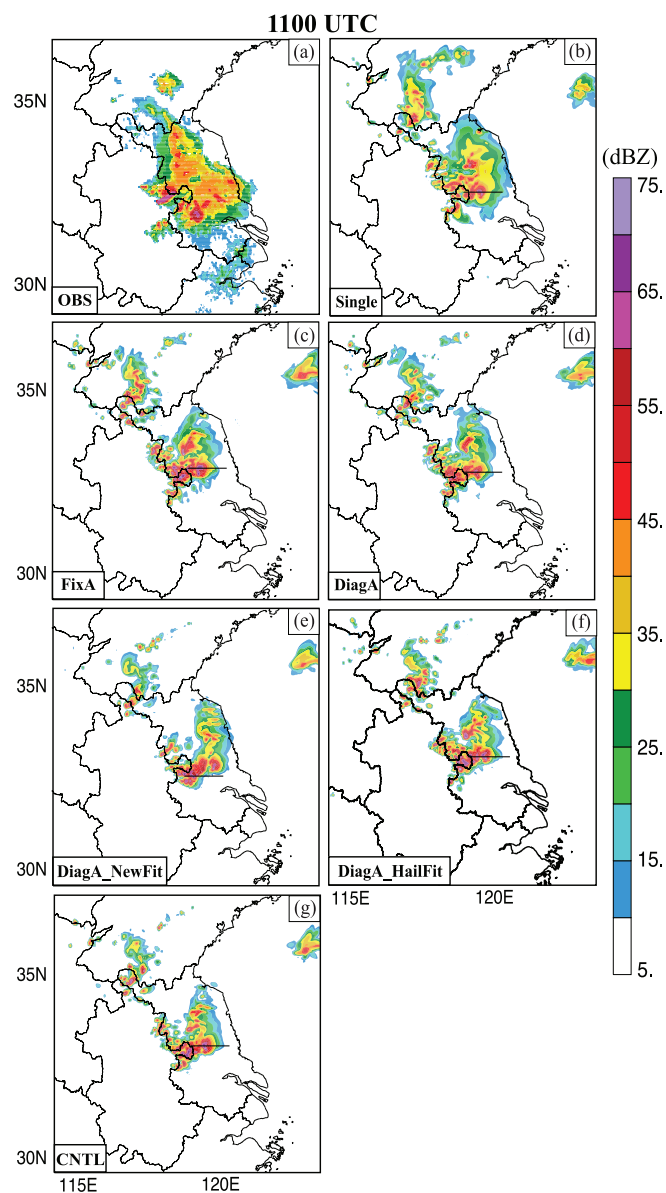


**Fig. 3.** Composite (column-maximum) radar reflectivity (dBZ) from (a) operational radar observations, and experiments using various configurations of the MY schemes, including experiments (b) Single, (c) FixA, (d) DiagA, (e) DiagA\_NewFit, (f) DiagA\_HailFit and (g) CNTL, at 1100 UTC 28 April 2015.

the surface from a weighted integration of radar reflectivity exceeding 40 dBZ above the melting level, and it can be calculated from both three-dimensional observed radar reflectivity and from model simulated reflectivity. However, given the reliance of MESH on the reflectivity above the melting level, there are clear uncertainties in such an estimation so it may be considered a proxy for actual maximum hail size at the surface for forecast evaluation purpose here. In the next two subsections, we will also examine alternative ways of estimating surface hail mass, hail number, and maximum hail size.

Fig. 4 presents the swaths of MESH derived from radar observations and simulations using various MP schemes at 1-km grid spacing between 0600 and 1600 UTC at 5-min intervals. As noted in L18, the radar-derived MESH ranging from 35 to 50 mm (Fig. 4a) is generally consistent with the hailstones observations reported by CMA. It was also found that MESH derived from the CNTL produced higher fractional skill scores than Single, FixA and DiagA (c.f., Fig. 9 in L18), although some underestimation of MESH values still exists in CNTL within the southern

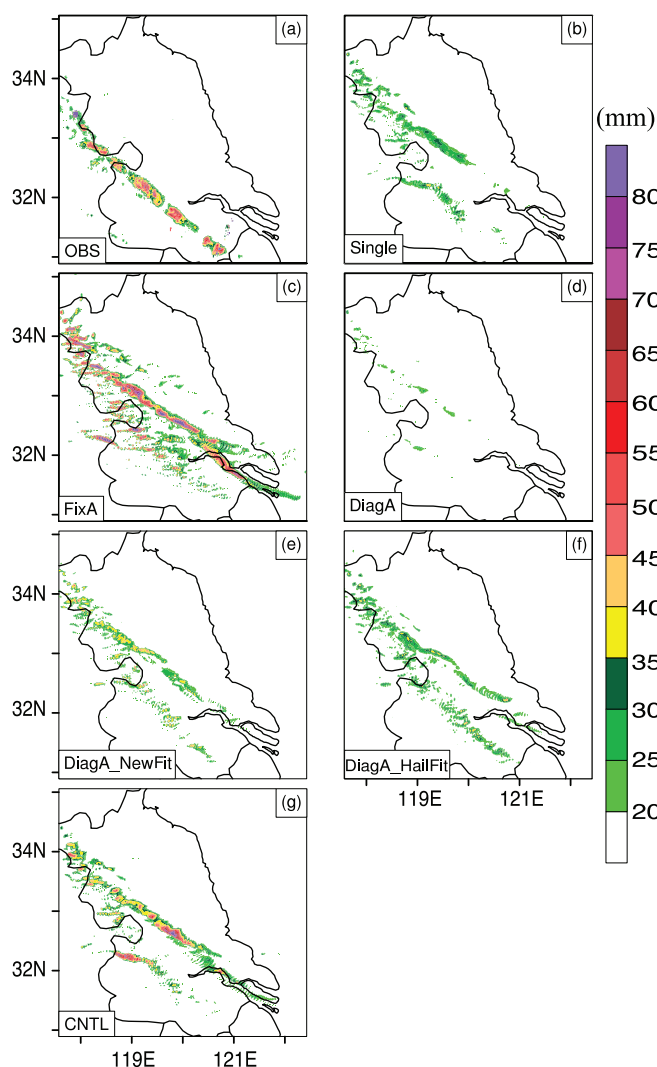


**Fig. 4.** Maximum estimated size of hail (MESH) (mm) derived from (a) the operational radar observations, and experiments using different MY schemes, including (b) Single, (c) FixA, (d) DiagA, (e) DiagA\_NewFit, (f) DiagA\_HailFit and (g) CNTL. MESH fields are calculated for the inner domain at 1-km grid resolution between 0600 and 1600 UTC 28 April 2015 at five-min intervals.

portion of the swath (Figs. 4a, g).

Compared to other experiments using one- or two-moment schemes, DiagA\_NewFit reproduces the MESH swath of CNTL the best, generating several centres of MESH approaching 40 mm (Figs. 4e, g). Overall, the MESH values in DiagA\_NewFit are lower than those of CNTL though, but not as low as those of Single and DiagA. This is also consistent with the predicted radar reflectivity from DiagA\_NewFit that is generally the closest to that of CNTL (Figs. 3e, g). Notably, DiagA\_HailFit produces smaller values of MESH below 35 mm than DiagA\_NewFit and CNTL (Figs. 4e, f, g); however, its corresponding radar reflectivity is over-estimated (Figs. 3e, f, g). This suggests that larger quantities of smaller-sized hailstones are generated in DiagA\_HailFit than in DiagA\_NewFit, consistent with the PSD analyses to be presented in Section 5.3 later.

### 5.2.2. SAHNC and SAHM

The total kinetic energy from hail falling to the ground determines to a large extent the destructiveness of a hailstorm. In this respect, L18 proposed the surface accumulated hail number concentration (SAHNC) parameter, which can be used to identify the number of surface accumulated hailstones larger than a specific size. Given that no high-quality in-situ hail count and mass observations are available, inter-

comparisons are performed among experiments using the various MP schemes, taking reports from CMA as references.

The SAHNC swaths for hail diameter thresholds of 30 and 40 mm (SAHNC30/40) from all experiments are shown in Figs. 5 and 6. As concluded in L18, the surface accumulated SAHNC30/40 and total mass from CNTL are consistent with the accumulated hail depth exceeding 10 cm over some areas according to CMA report and photographs taken during this event, corresponding to a number of  $10^3$ – $10^4$   $m^{-2}$  for hail larger than 4 cm. The significant overestimation and underestimation of SAHNC from FixA, and Single and DiagA, respectively, are generally consistent with their corresponding MESH and radar reflectivity fields (L18).

In comparison to FixA, DiagA\_NewFit produces similar SAHNC30/40 extents and the same orders of magnitudes ( $\sim 10^4$ – $10^6$  and  $10^2$ – $10^5$   $m^{-2}$ ) for intense hailfall regions compared to CNTL (Figs. 5d, f, 6d, f). Thus, the new  $\alpha$ - $D_m$  relations improve the explicit forecasts of hail number concentrations at the surface compared with the other one- or two-moment schemes. Moreover, the SAHNC30/40 of DiagA\_HailFit (Figs. 5e, 6e) are about one order of magnitude smaller than those of DiagA\_NewFit at some parts of the swaths, consistent with its slight underestimation of MESH (Fig. 4f). These results indicate that the newly derived relations for rain and graupel also play important roles in improving the prediction of hail size and total number accumulation at the surface.

Aside from SAHNC, SAHM during the hailstorm's lifespan between 0600 and 1600 UTC is also compared among the experiments. For example, compared against CNTL (Fig. 7f), Single and DiagA underestimate SAHM at the ground (Figs. 7a, c); FixA produces twice the width of SAHM swath compared to CNTL (Fig. 7b) (L18). The SAHM range and

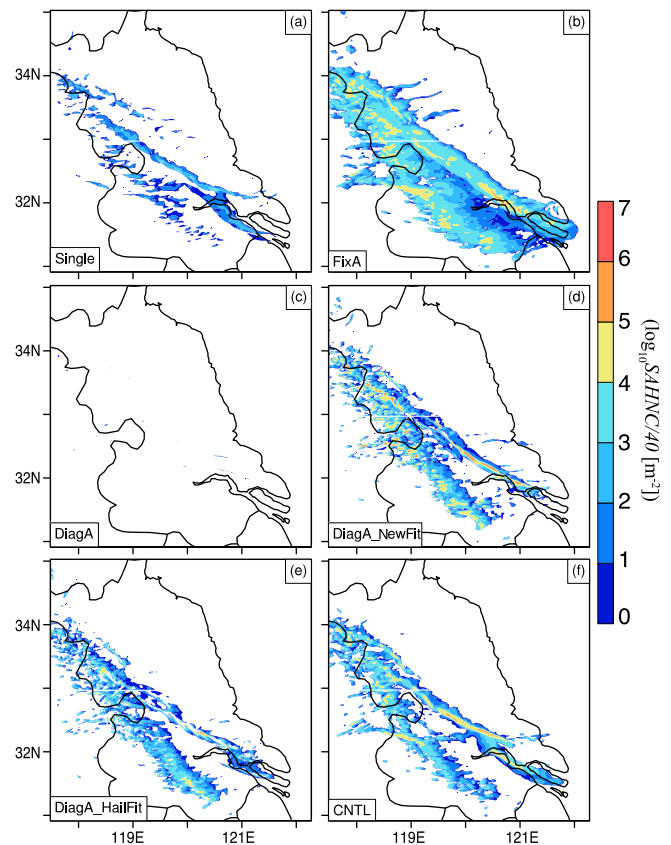


Fig. 6. As in Fig. 5, but for SAHNC with hail diameters exceeding 40 mm.

peak values ( $\sim 80$  mm) in both DiagA\_NewFit and DiagA\_HailFit are closer to that of CNTL than FixA, although it is somewhat underestimated over some portions of the swaths (Figs. 7d–f). Moreover, the SAHM generated by DiagA\_HailFit is 10–20 mm higher than that by DiagA\_NewFit, especially over the southern portions of the swaths (Figs. 7d–e). The larger SAHM in DiagA\_HailFit should mainly come from smaller-sized hailstones with diameters below 30 mm (c.f., Figs. 4f, 5, 6e). More physical explanations for the differences in the hail predictions among FixA, DiagA\_HailFit and DiagA\_NewFit are investigated via PSD examinations and microphysical budget analyses in the next two subsections.

### 5.3. Hail size distributions within simulations

To help understand the reasons for the differences in hail prediction skills among the experiments using various MP schemes, hail size distributions within the simulated storms are examined. Figs. 8 and 9 show vertical cross-sections of the hail mixing ratio ( $Q_h$ ) and total number concentration ( $N_{Th}$ ), and the maximum hail size ( $D_{max}$ ) and radar reflectivity ( $Z$ ), respectively, for all experiments. Following MY06a and L18,  $D_{max}$  is defined as the maximum hail size for which the total number of hailstones larger than  $D_{max}$  is equal to a threshold number of  $N_{Th}$ ; the threshold value is set to be  $10^{-4}$   $m^{-3}$ . The cross-sections are taken from west to east through the primary hail-mass core within the storms at 1100 UTC of each experiment, as indicated by the solid black lines in Figs. 3b–f. As particle size spectra have direct effects on most microphysical processes, the size spectra of hail, graupel and rain particles at low and high levels from all experiments are also examined (Fig. 10).

Significant differences in the simulated PSDs are exhibited among the experiments using various MP schemes. For example, it was noted in L18 that as Single only predicts  $Q_x$ , the corresponding  $N_{Tx}$  and  $Z_x$  are diagnostically related to  $Q_x$ ; the  $Q_x$ ,  $N_{Tx}$  and  $Z_x$  of Single are generally

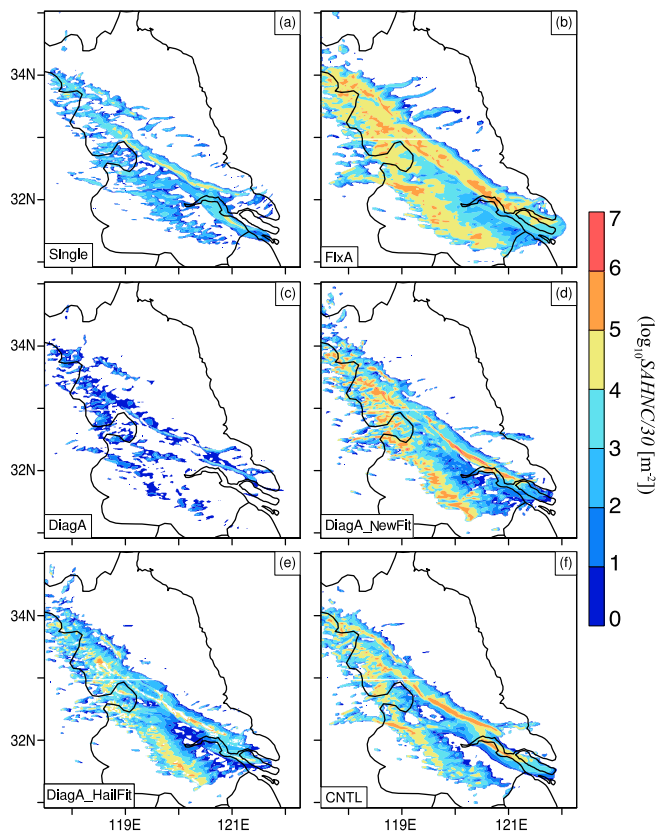


Fig. 5. Surface accumulated hail number concentration (SAHNC) with hail diameters exceeding 30 mm (in a base-10 logarithmic scale;  $m^{-2}$ ) from experiments (a) Single, (b) FixA, (c) DiagA, (d) DiagA\_NewFit, (e) DiagA\_HailFit and (f) CNTL, between 0600 and 1600 UTC for the inner domain at 1-km resolution.

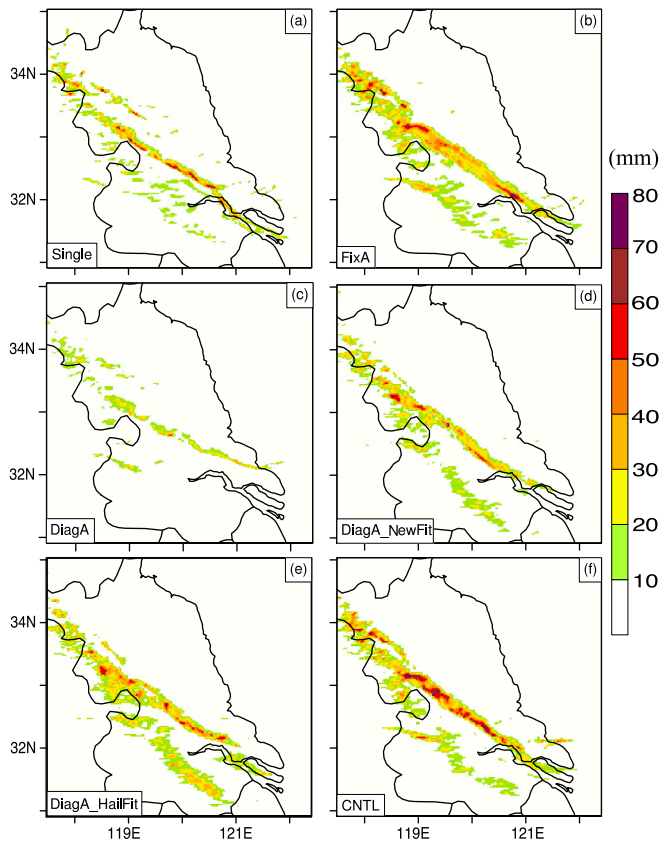


Fig. 7. SAHM in water-equivalent depth (mm) between 0600 and 1600 UTC 28 April 2015 from experiments (a) Single, (b) FixA, (c) DiagA, (d) DiagA\_NewFit, (e) DiagA\_HailFit and (f) CNTL, for the inner domain at 1-km grid spacing.

collocated (Figs. 8a, 9a). The hail particles in the storm from Single examined herein also show homogeneous sizes around 0.04 mm from low to high levels (Figs. 9a, 10a–b), since no size sorting of hydrometeors can be represented in one-moment scheme (MY05a; L18). For the same reason, the graupel size at the high level from Single is also significantly overestimated compared with experiments using multi-moment schemes (Fig. 10d). The particle sizes of hail, graupel and rain at the low level from FixA using  $\alpha = 0$  for all hydrometeors are significantly larger than those of CNTL (Figs. 9b, 10a, c, e). However, due to the overestimation of  $\alpha$  for hail, graupel and rain in DiagA compared to CNTL (Figs. 15a–c), their size sorting effects are strongly suppressed (MY05a; L18), so that the particle sizes at lower levels in DiagA are much smaller (Figs. 9c, 10c–e).

DiagA\_HailFit overpredicts the  $N_{Th}$  values within the storm compared to FixA and DiagA\_NewFit while generating  $Q_h$  close to DiagA\_NewFit (Figs. 8b, d, e). Thus, the hailstones produced by DiagA\_HailFit are smaller than by FixA and DiagA\_NewFit (Figs. 9b, d, e, 10a–b). These are also consistent with its underestimation of MESH and SAHNC30/40 as aforementioned (c.f., Figs. 4f, 5e, 6e). On the contrary, the rain and graupel sizes at low levels from DiagA\_HailFit are even larger than those of FixA (Figs. 10c, e), due to the excessive size sorting of graupel and rain (MY05a). These also contribute to the larger radar reflectivity over the areas of stratiform clouds in DiagA\_HailFit compared to DiagA\_NewFit (c.f., Figs. 3e–f). Moreover, the peak values of  $Q_h$  and  $N_{Th}$  in DiagA\_NewFit are  $\sim 11 \text{ g m}^{-3}$  and  $10^{3.5} \text{ m}^{-3}$ , closer to those of CNTL than FixA and DiagA\_HailFit (Figs. 8b, d, e, f). In particular, the vertical distribution of  $D_{max}$  from DiagA\_NewFit, with its peaks of 80–100 mm below the freezing level, is the closest to that of CNTL (Figs. 9d, f). The hail, graupel and rain particle size spectra at the low and high levels within the storm in CNTL are also the best reproduced by DiagA\_NewFit, although there are still slight underestimation

in hail and graupel size at the low levels (Figs. 10a, c, e).

#### 5.4. Differences in simulated microphysical processes

To gain additional physical insights into the differences among the experiments, detailed microphysical budget analyses are performed. Besides adding hail mass budget analyses for DiagA\_NewFit and DiagA\_HailFit based on that in L18, mass budget analyses are also performed for graupel and rain to examine the effects of their  $\alpha$ - $D_m$  relations and corresponding impacts on hail prediction. The mass budget analyses are based on the corresponding prediction equations of MY scheme (c.f., eqs. A7, A6, A3 in MY05b). As noted in L18, the dominant microphysical processes responsible for hail mass growth in this hailstorm are hail collection of cloud water ( $QCL_{ch}$ ), collection of rain ( $QCL_{rh}$ ) and melting of hail ( $QML_{hr}$ ); other microphysical processes are minimal. It is also found herein that the dominant processes for graupel are graupel collection of cloud ( $QCL_{cg}$ ) and melting of graupel ( $QML_{gr}$ ); the dominant rainwater processes are melting of graupel ( $QML_{gr}$ ) and hail ( $QML_{hr}$ ), and collection by hail ( $QCL_{rh}$ ). Mass productions from other processes for graupel and rain are minimal.

Figs. 11–13 depict the time series of domain-total mass and dominant mass production rates for hail, graupel and rain at 1-km grid spacing between 0600 and 1600 UTC for multi-moment experiments. The profiles of dominant process rates are shown in Fig. 14. Finally, the accuracies of the new  $\alpha$  relations for hail, graupel and rain are also assessed (Fig. 15). Since the PSD features within Single are unreasonable (c.f., Figs. 8, 9a, 10) and the corresponding process rates differ significantly, its results are not included in the plots.

As concluded in L18, the domain-total hail mass is significantly overestimated by FixA (Fig. 11a,  $\sim 6.2 \times 10^5$  Kilon at 0940 UTC), primarily contributed by its higher  $QCL_{ch}$  rate at higher levels above 3 km MSL (Figs. 11b, 14a); on the contrary, the  $QCL_{ch}$  and  $QML_{hr}$  rates by DiagA are much lower than those of CNTL (Figs. 11b, d). Besides, the domain-total graupel mass from FixA is  $\sim 0.2 \times 10^4$  Kilon less than that of CNTL (Fig. 12a), due to the counteracting effects of lower  $QCL_{cg}$  and  $QML_{gr}$  rates at upper and lower levels, respectively (Figs. 12b–c, 14b). The lower  $QCL_{cg}$  rate in FixA with larger graupel sizes may be primarily compensated by its larger  $QCL_{ch}$  (Fig. 11b), and the lower rate of  $QML_{gr}$  is assumed to be related to slower melting of larger-sized graupel particles (Fig. 10c). The underestimated  $QML_{gr}$ , overestimated  $QML_{hr}$  and  $QCL_{rh}$  within low levels by FixA result in slightly larger domain-total rain mass than CNTL (Figs. 13a–d, 14c). Moreover, the domain-total graupel mass,  $QCL_{cg}$  and  $QML_{gr}$  from DiagA are all underestimated compared with those of CNTL (Figs. 12a–c). Consequently, to achieve water mass conservation within the model domain, larger domain-total rain mass is produced in DiagA (Fig. 13a), although with smaller rain particle sizes at lower levels (Fig. 10e).

DiagA\_HailFit predicts less domain-total hail mass compared to DiagA\_NewFit (Fig. 11a), resulting from the smaller  $QCL_{ch}$  aloft, smaller  $QCL_{rh}$  and larger  $QML_{hr}$  at lower levels (Figs. 11b–d, 14a). The smaller  $QCL_{ch}$ ,  $QCL_{rh}$  and larger  $QML_{hr}$  from DiagA\_HailFit are also consistent with its smaller  $D_{max}$  within the storm and smaller MESH values on the surface than DiagA\_NewFit (Figs. 4e–f, 9c–d). In addition, DiagA\_HailFit predicts smaller domain-total graupel mass, with lower  $QCL_{cg}$  and  $QML_{gr}$  than DiagA\_NewFit (Figs. 12a–c, 14b). The lower  $QML_{gr}$  in DiagA\_HailFit is related to its larger sizes of graupel at low levels due to excessive size sorting, where graupel melting is less efficient (Fig. 10c). The domain-total rain mass of DiagA\_HailFit is larger than that of DiagA\_NewFit, primarily resulting from the higher  $QML_{hr}$  and lower  $QCL_{rh}$  within lower levels (Figs. 13a–d, 14c). The fixed  $\alpha$  of zero for rain in DiagA\_HailFit also leads to even larger raindrop sizes at lower levels than FixA (Figs. 10e, 15c) due to excessive size sorting of rain (MY05a).

Moreover, the domain-total hail mass from DiagA\_NewFit and its dominant mass rates are the closest to those of CNTL among the experiments, although there still exist some overestimation of  $QML_{hr}$  within lower levels (Figs. 11a–d, 14a). This is also consistent with its

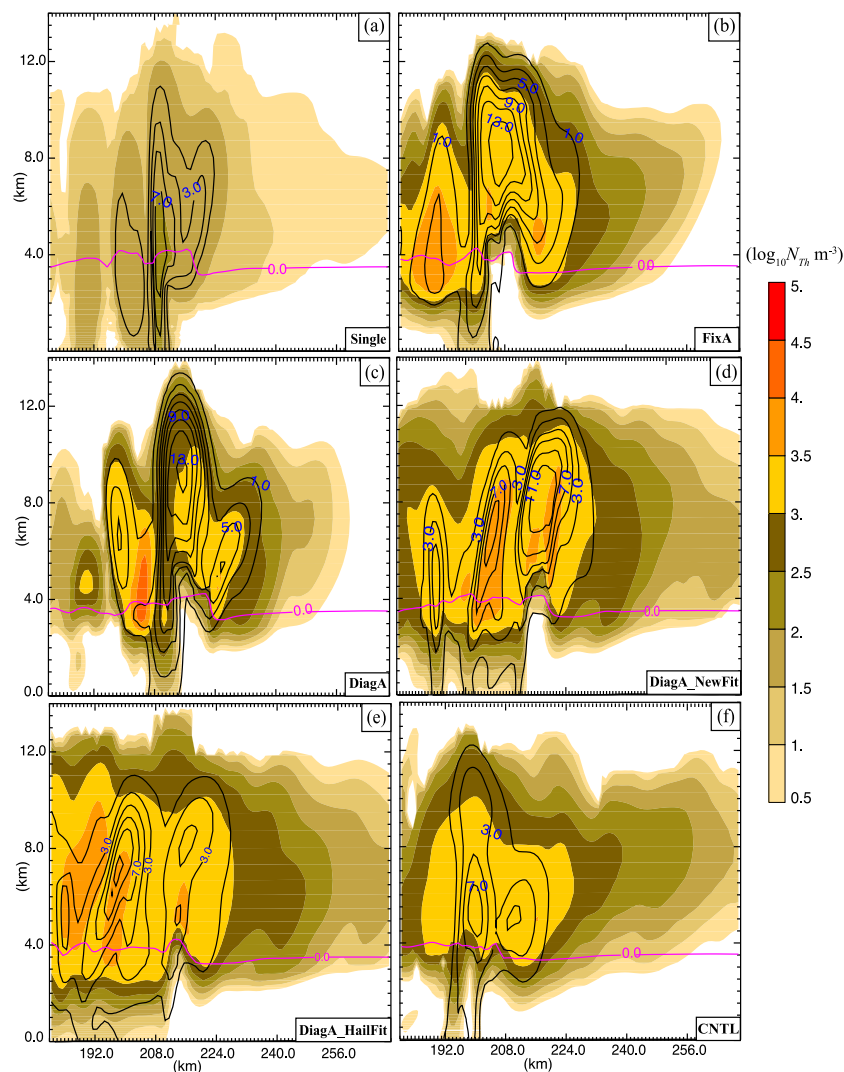


**Fig. 8.** Vertical cross-sections of hail total number concentration (shaded, in a base-10 logarithmic scale,  $\text{m}^{-3}$ ) and mass mixing ratio (black contours,  $\text{g m}^{-3}$ ) at 1100 UTC from experiments (a) Single, (b) FixA, (c) DiagA, (d) DiagA\_NewFit, (e) DiagA\_HailFit and (f) CNTL. The magenta contours denote the freezing level. The cross sections are taken through the primary hail mass cores of storms indicated by the black lines in Fig. 3.

slight underestimation of MESH and surface hail mass as discussed before (Figs. 4e, 7d). The domain-total graupel mass, the corresponding  $QCL_{cg}$  and  $QML_{gr}$  rates from DiagA\_NewFit are also closer to those of CNTL than FixA and DiagA\_HailFit (Fig. 12), the same as for rain category (Fig. 13). Primarily ascribed to the overestimation of  $QML_{hr}$  within lower levels from DiagA\_NewFit (Figs. 13c, 14c), domain-total rain mass from DiagA\_NewFit is slightly overestimated than that of CNTL (Fig. 13a).

The mean  $\alpha$  values for hail from DiagA\_NewFit and CNTL increase from approximately zero to  $\sim 0.5$  between 4 km and 3 km MSL slightly while the  $\alpha$  increases much more rapidly from 3 km towards the surface (Fig. 15a). The lower increase rate of mean  $\alpha$  for hail between 4 km and 3 km MSL than the levels below represents a wider hail particle size distribution (PSD) due to the mixing of  $QCL_{ch}$  and  $QCL_{rh}$  (i.e., the riming and wet growth of hail) within the clouds (Fig. 14a). On the other hand, the rapid increase of mean  $\alpha$  for hail below 3 km MSL (around the height of melting level), indicating a rapid narrowing PSD, which is more likely related to the strong  $QCL_{rh}$  (i.e., the wet growth of hail) and  $QML_{hr}$  (Fig. 14a). The mean  $\alpha$  for graupel remains at  $\sim 0.5$  above 3 km MSL, and increases slightly from  $\sim 3$  km MSL towards the surface (Fig. 15b), representing narrowing PSD of graupel due to  $QML_{gr}$  and size sorting of graupel; for rain, the  $\alpha$  values range from 0.2 to 0.5 (Fig. 15c). The  $\alpha$  for

rain from DiagA\_NewFit is slightly smaller than that of CNTL, consistent with its wider rain size spectra than CNTL (Fig. 10e). The differences in  $\alpha$  between DiagA\_NewFit and CNTL may be at least partially attributed to the limitations of raindrop breakup process in the MY three-moment scheme, so as their differences in the rain mass budget analyses, as discussed earlier.

Moreover, the larger values of  $\alpha$  in DiagA\_NewFit compared with the fixed  $\alpha$  of zero in FixA and DiagA\_HailFit represent narrower PSD, with fewer large particles in the PSD tail. In this way, collection growth of particles in DiagA\_NewFit, e.g.,  $QCL_{rh}$  rate is significantly limited than in FixA below 4 km MSL (Figs. 11b–c). The excessive size sorting in FixA is also curtailed in DiagA\_NewFit, as its larger diagnostic values of  $\alpha$  can determine a smaller size sorting ratio. On the other hand, the mean  $\alpha$  values for hail and rain do not decrease rapidly with height and maintain at  $\sim 3$  above 3 km MSL in DiagA (Figs. 15a, c); its mean  $\alpha$  for graupel decreases rapidly from  $\sim 12$  near the surface to  $\sim 3$  at around 3 km MSL and remains at  $\sim 3$  above (Fig. 15b). Thus, it is clear that DiagA\_NewFit better reproduces the vertical variations of  $\alpha$  for hail, graupel and rain in CNTL than other experiments.

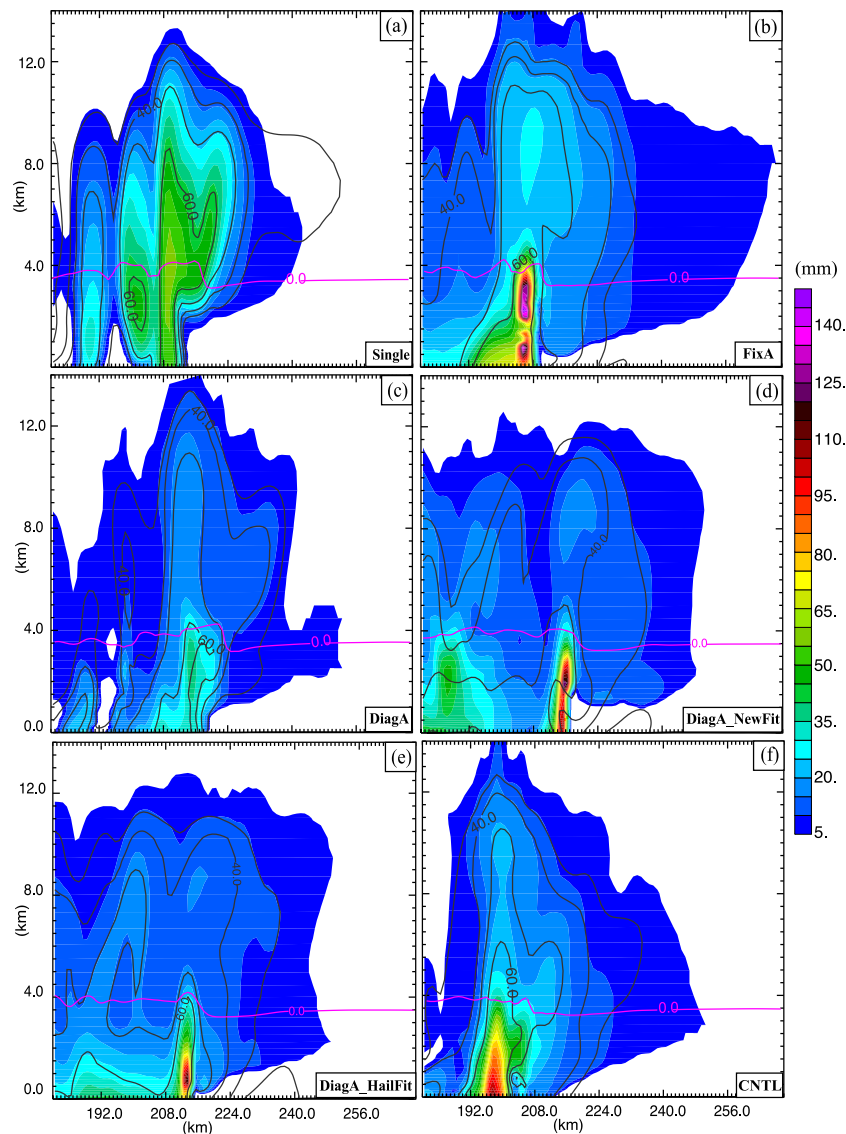


Fig. 9. As in Fig. 8, but for vertical cross-sections of  $D_{max}$  (shaded, mm) and radar reflectivity (black contours, dBZ).

## 6. Summary and conclusions

In this study, new relations between the shape parameter  $\alpha$  of gamma PSD and the mean-mass diameter  $D_m$  for the rain, graupel and hail hydrometeor categories are derived based on the simulation of a real severe hailstorm case in eastern China on 28 April 2015 at 1-km horizontal grid spacing using the three-moment MY microphysics scheme with the ARPS model. During the hailstorm event, a number of egg-sized hailstones were reported over Jiangsu Province, along with intense lightning and damaging surface winds. Simulation using the three-moment scheme is taken as a reference, as previous studies have noted that three-moment schemes can directly predict three free parameters of the gamma size distribution and best reproduce the observed storm evolution compared with other schemes. This approach is also motivated by earlier studies that found strong relations between  $\alpha$  and  $D_m$ , and the fact that two-moment schemes using diagnostic  $\alpha$  can produce results closer to three-moment schemes than corresponding two-moment schemes using fixed values of  $\alpha$ . The least-squares polynomial fit is applied to the averaged  $\alpha$  and  $D_m$  within ten bins, which are predefined based on  $D_m$ . However, it is also noted that more accurate parameterizations of the microphysical processes in MY three-moment scheme are still in need, e.g., the raindrop breakup and snow fragmentation processes, that will be

further improved in future studies.

The new  $\alpha$ - $D_m$  relations are implemented into the MY two-moment scheme. To investigate its impacts on hail prediction, experiments using one-, two- and three-moment schemes are performed for the Jiangsu hailstorm at 1-km grid spacing. The experiment using the three-moment scheme is taken as the control simulation (referred to as CNTL). Five experiments are performed: experiment Single using the one-moment scheme and other four experiments using the two-moment schemes, with fixed  $\alpha$  of zero in FixA, diagnostic  $\alpha$  based on the  $\alpha$ - $D_m$  relations from MY05a in DiagA, the new diagnostic relations for hail, graupel and rain in DiaA\_NewFit, and new  $\alpha$  relation for hail only in DiaA\_HailFit. First, verifications against operational radar observations indicate that all experiments can generally capture the overall structure and evolution of the hailstorm. However, substantial differences exist in the simulated storm intensities among the experiments using the various microphysics schemes. For example, DiagA\_HailFit generates larger reflectivity values over areas of stratiform clouds than DiagA\_NewFit does, and DiagA\_NewFit predicts radar reflectivity that is closest to that of CNTL among all experiments.

Hail predictions of the experiments in terms of MESH, SAHNC, and SAHM are examined. Compared to other experiments using one- and two-moment schemes, DiagA\_NewFit best reproduces MESH based on

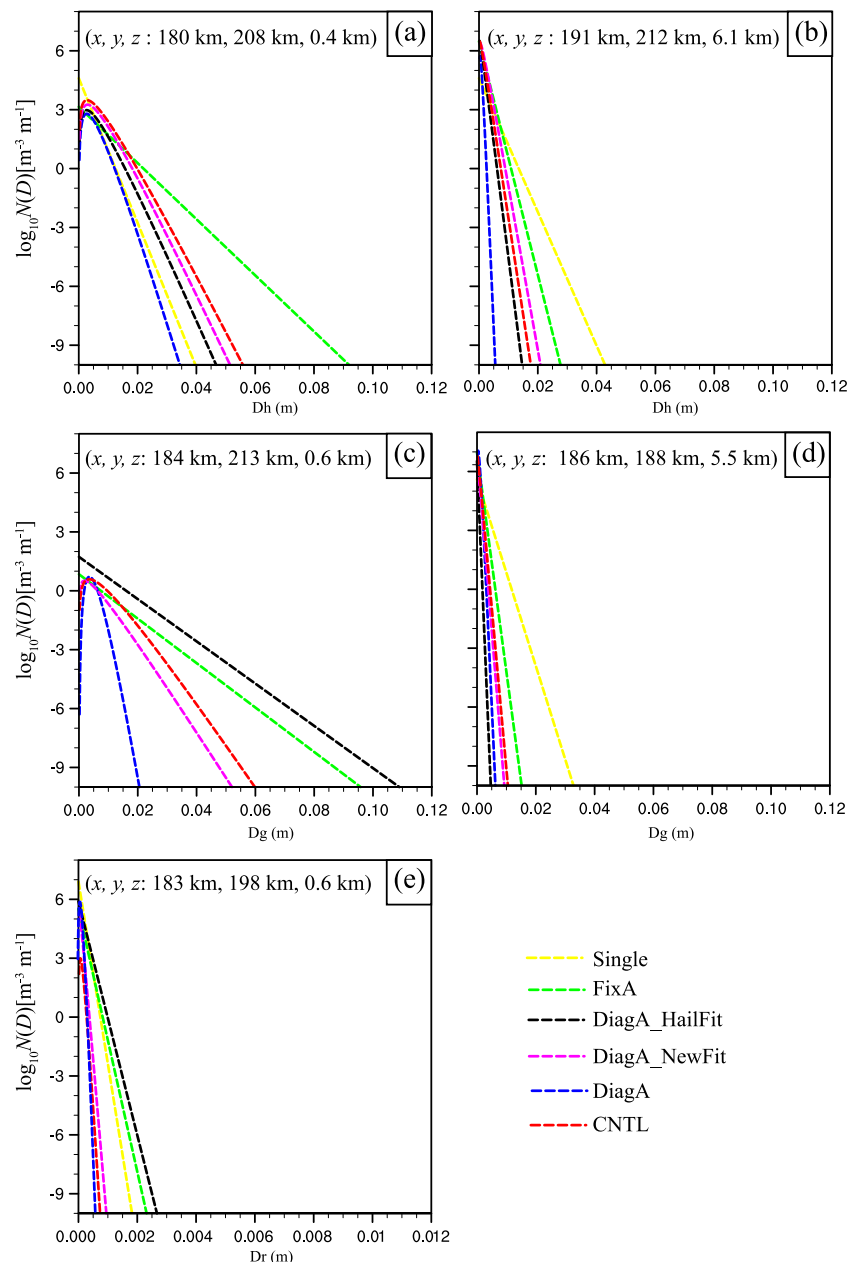


**Fig. 10.** Particle size distributions for hail (a–b), graupel (c–d) and rain (e) at different lower and higher levels within the storms at 1100 UTC from experiments Single, FixA, DiagA\_HailFit, DiagA\_NewFit, DiagA and CNTL.

radar observations and MESH from CNTL, yielding values ranging from 35 to 50 mm. The SAHNC30/40 in DiagA\_NewFit are of the same orders of magnitudes as in CNTL, although the corresponding SAHM is somewhat underestimated over several parts of the SAHM swaths. In contrast, DiagA\_HailFit produces smaller MESH (below 35 mm) and SAHNC30/40 values than DiagA\_NewFit, indicating that the newly derived relations for rain and graupel also contribute to improving hail size and total number predictions. Note that there still exist some uncertainties in the comparisons of the simulated radar reflectivity and the model-derived MESH against the radar observed reflectivity and the corresponding radar-derived MESH. The direct comparisons of the model simulations against the observed hail size should be ideal; however, reliable hail size observation datasets are not available.

Examinations of PSDs in the storms show that both hail and graupel particles aloft in Single have unreasonably large sizes compared to experiments using multi-moment schemes, as no size sorting of

hydrometeors is represented when only the mass moment is predicted. Excessive size sorting of hail, graupel and rain in FixA with  $\alpha = 0$  for all hydrometeors contributes to the significantly overestimated particle sizes at lower levels. On the contrary, the hail, graupel and rain particle sizes at lower levels in DiagA are much smaller than those in CNTL as size sorting is strongly suppressed with overestimated  $\alpha$ . DiagA\_HailFit generates smaller hail sizes within the storm compared to DiagA\_NewFit, consistent with its smaller MESH and SAHNC. The rain and graupel sizes predicted by DiagA\_HailFit are significantly overestimated at lower levels, which are even larger than in FixA, responsible for the overestimation of radar reflectivity over the areas of stratiform clouds. Generally speaking, the hail, graupel and rain PSD features within the storm of DiagA\_NewFit are the closest to those of CNTL.

Detailed microphysical budget analyses are also performed for dominant microphysical processes contributing to hydrometeor mass growth. The domain-total hail mass is significantly overestimated by

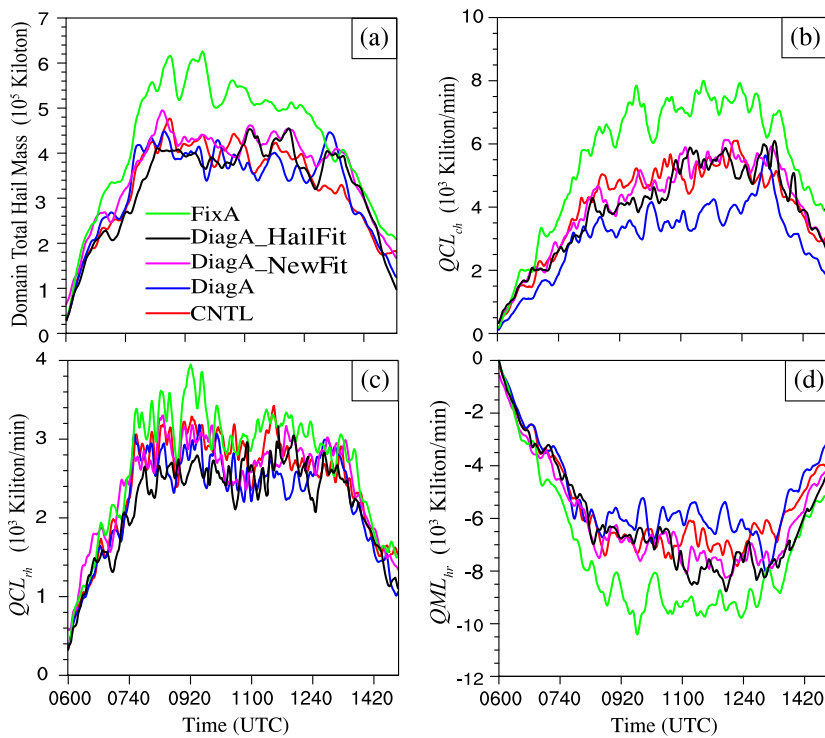


**Fig. 11.** Time series of domain-total (a) hail mass over the inner domain at 1-km resolution and (b-d) rates of dominant microphysical processes responsible for hail production between 0600 and 1600 UTC for experiments using multi-moment schemes, i.e., FixA, DiagA\_HailFit, DiagA\_NewFit, DiagA and CNTL. The dominant microphysical processes include hail collection of cloud water ( $QCL_{ch}$ , panel b), collection of rainwater ( $QCL_{rh}$ , panel c), and melting of hail ( $QML_{hr}$ , panel d). Hail mass contribution from other microphysical processes are minimal and not shown.

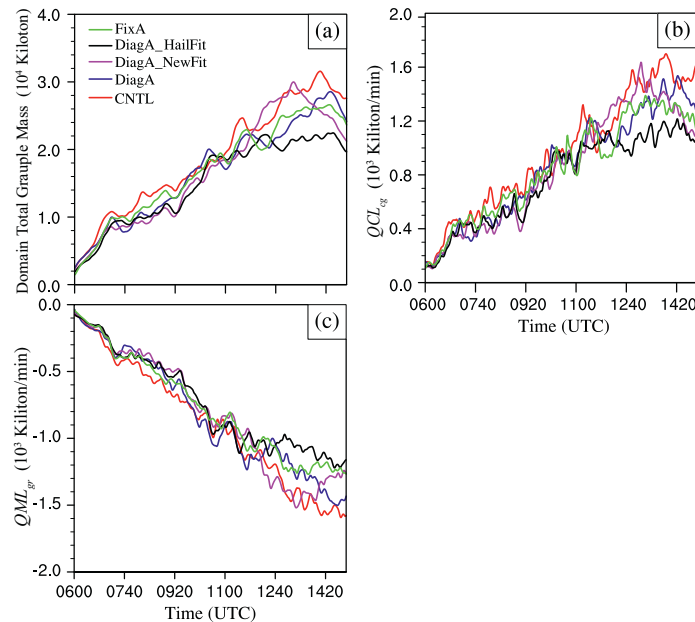


**Fig. 12.** As in Fig. 11, but for time series of domain-total (a) graupel mass, and (b-c) rates of dominant microphysical processes responsible for graupel mass production. The dominant microphysical processes include graupel collection of cloud water ( $QCL_{cg}$ , panel b) and melting of graupel ( $QML_{gr}$ , panel c). Other microphysical processes contributions to graupel mass are minimal and not shown.

FixA, and its graupel mass is underestimated. The domain-total hail and graupel mass are underestimated in DiagA, and the rain mass is overestimated compared to CNTL, generating underestimated particle sizes of hail, graupel and rain. Besides, DiagA\_HailFit predicts less domain-total hail and graupel mass, and larger rain mass compared with DiagA\_NewFit, with lower  $QML_{gr}$  related to its larger graupel size at lower levels due to excessive size sorting. Above all, DiagA\_NewFit predicts the closet domain-total mass and microphysical processes to CNTL, although the  $QML_{hr}$  is slightly higher than CNTL. Furthermore,

DiagA\_NewFit well reproduces the vertical variations of  $\alpha$  for hail, graupel and rain of those from CNTL, albeit the mean  $\alpha$  values from DiagA\_NewFit are slightly smaller than the corresponding values from CNTL.

This study serves as proof that the use of diagnostic relations of  $\alpha$  derived from a real case simulation using a three-moment scheme can improve two-moment scheme simulations, enabling them to reproduce storm intensities and hail predictions that is almost on a par with those using a three-moment scheme, whilst retaining the computational

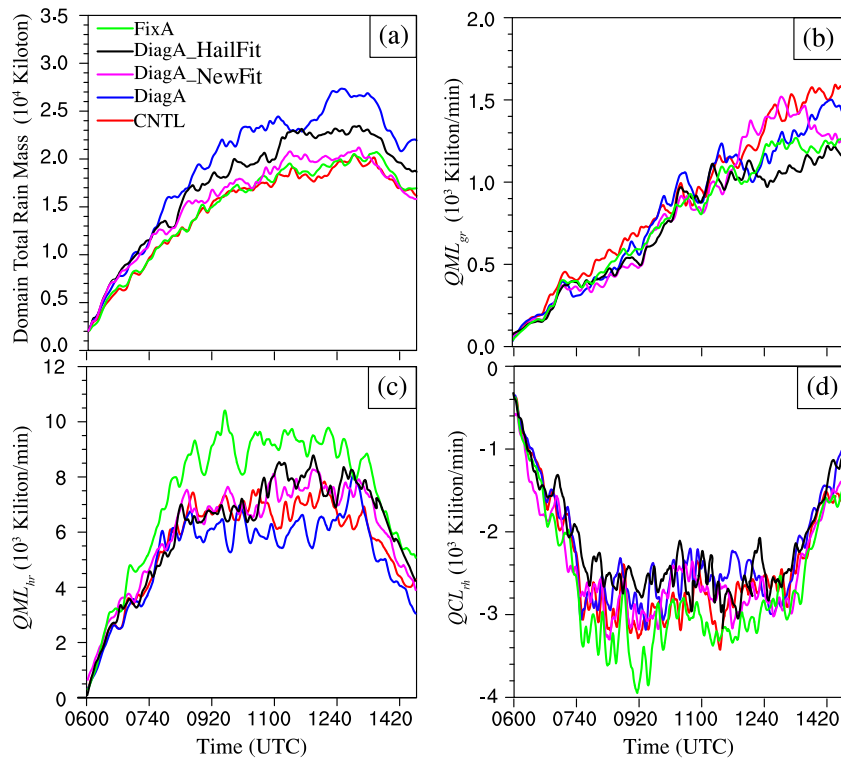


**Fig. 13.** As in Fig. 11, but for time series of domain-total (a) rain mass, and (b–d) rates of dominant microphysical processes responsible for rain production. The dominant microphysical processes include: melting of graupel and hail ( $QML_{gr}$  and  $QML_{hr}$ , panels b–c), hail collection of rain ( $QCL_{rh}$ , panel d). Other microphysical processes contributions to rain mass are minimal.

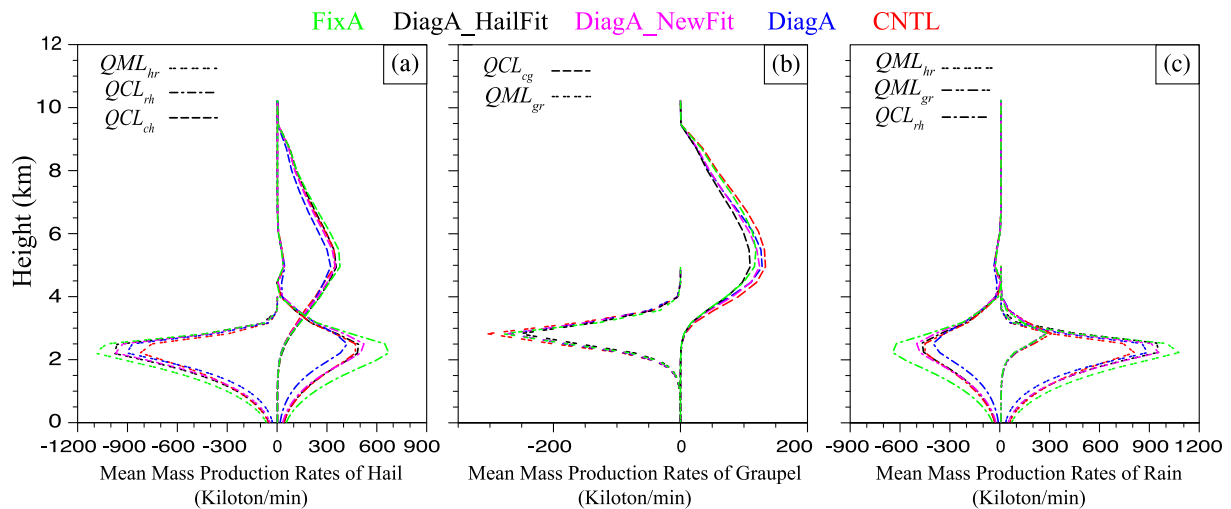


**Fig. 14.** Rate profiles of the dominant microphysical processes from experiments FixA, DiagA\_HailFit, DiagA\_NewFit, DiagA and CNTL for (a) hail mass production, including  $QCL_{ch}$ ,  $QCL_{rh}$  and  $QML_{hr}$ , (b) graupel mass production, including  $QCL_{cg}$  and  $QML_{gr}$ , and (c) rain mass production, including  $QML_{gr}$ ,  $QML_{hr}$  and  $QCL_{rh}$ . The microphysical rates are averaged horizontally within the hailstorm for the inner 1-km domain between 0600 and 1600 UTC 28 April 2015 at 1-min intervals.

efficiency of the two-moment scheme. While similar studies have been attempted before, the existing studies have been performed under much more idealized settings. Even though the results presented in this paper are based on a single case, we have applied the diagnostic  $\alpha$  relations derived in this current study to the pulse-type hailstorm studied earlier in L17. The experiment using the new  $\alpha$  relations predicts closer MESH swaths to the experiment using three-moment scheme than all other experiments using one- or two-moment schemes for that case also, although there is underestimation in MESH values in that case too (not shown). Given that the  $\alpha$  relations were obtained by fitting to simulation

data of one hailstorm case, and improved results are also obtained when applied to a different case, the efficacy of such an approach is demonstrated. It is possible that more generally applicable relations could be obtained by fitting to three-moment simulation data of multiple cases, then such relations can be tested for different types of precipitation systems under different atmospheric conditions. These are topics for future studies.

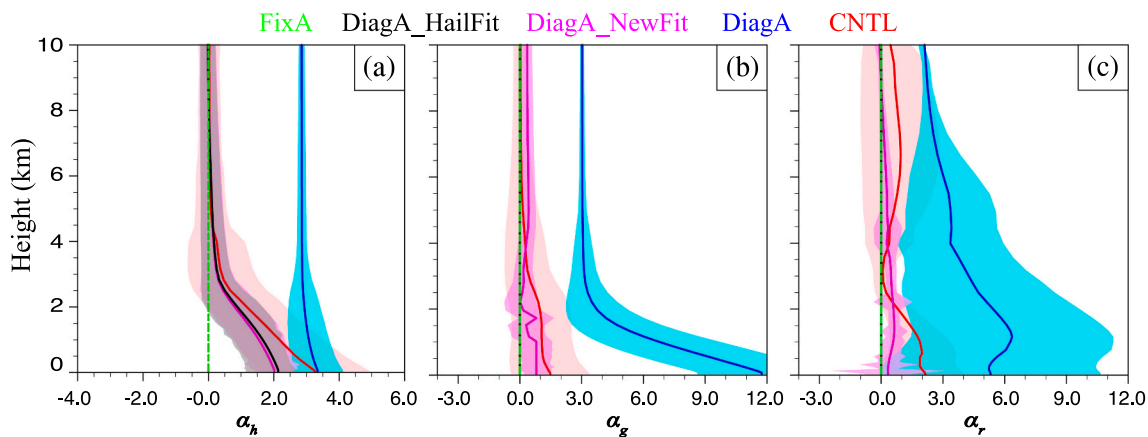


**Fig. 15.** Profiles of shape parameters of hail, graupel and rain from experiments FixA, DiagA\_HailFit, DiagA\_NewFit, DiagA and CNTL, averaged horizontally within the hailstorm for the inner 1-km domain between 0600 and 1600 UTC 28 April 2015 at 1-min intervals. The corresponding one standard deviations from the mean shape parameters profiles are shaded.

### Declaration of Competing Interest

The authors declare that they have no known competing financial interests or personal relationships that could have appeared to influence the work reported in this paper.

### Acknowledgements

This work was primarily supported by the National Research and Development Program of China (Grant 2018YFC1507303), the National Natural Science Foundation of China (Grants 419505044, 41730965 and 41975124), and the Jiangsu Province Entrepreneurship and Innovation Plan (Grant 2016/B19164). The NCEP 1° GFS final analysis data can be downloaded freely from <http://rda.ucar.edu/datasets/ds083.2/>. The radar dataset was provided by the Climate Data Center at the National Meteorological Information Center of the China Meteorological Administration. We gratefully acknowledge the High-Performance Computing Center (HPCC) of Nanjing University for carrying out the numerical calculations in this paper on its IBM Blade cluster system. The processed datasets within this paper, including the radar and NCEP 1° GFS final analysis datasets, are available at <http://drive.google.com/open?id=1fiFnaBnkW-VDKi4gGNo8L2RYVwtpdPCH>. The simulation results are stored at the HPCC and are available upon request.

### References

- Andrejczuk, M., Grabowski, W.W., Reisner, J., Gadian, A., 2010. Cloud-aerosol interactions for boundary layer stratocumulus in the Lagrangian Cloud Model. *J. Geophys. Res.-Atmos.* 115, D22214.
- Bae, S.-Y., Hong, S.-Y., Lim, K.-S.S., 2016. Coupling WRF double-moment 6-class microphysics schemes to RRTMG radiation scheme in Weather Research Forecasting Model. *Adv. Meteorol.* 2016, 5070154.
- Bae, S.-Y., Hong, S.-Y., Tao, W.-K., 2019. Development of a single-moment cloud microphysics scheme with prognostic hail for the Weather Research and Forecasting (WRF) Model. *Asia-Pac. J. Atmos. Sci.* 55, 233–245.
- Brandes, E.A., Zhang, G., Vivekanandan, J., 2002. Experiments in rainfall estimation with a polarimetric radar in a subtropical environment. *J. Appl. Meteorol.* 41, 674–685.
- Brdar, S., Seifert, A., 2018. McSnow: a Monte-Carlo particle model for riming and aggregation of ice particles in a multidimensional microphysical phase space. *J. Adv. Model. Earth Syst.* 10, 187–206.
- Cao, Q., Zhang, G., Brandes, E., Schuur, T., Ryzhkov, A., Ikeda, K., 2008. Analysis of video disdrometer and polarimetric radar data to characterize rain microphysics in Oklahoma. *J. Appl. Meteor. Climatol.* 47, 2238–2255.
- Chen, B., Yang, J., Pu, J., 2013. Statistical characteristics of raindrop size distribution in the Meiyu season observed in Eastern China. *J. Meteorol. Soc. Japan* 91, 215–227.
- Cholette, M., Morrison, H., Milbrandt, J., Thériault, J., 2019. Parameterization of the bulk liquid fraction on mixed-phase particles in the predicted particle properties (P3) scheme: Description and idealized simulations. *J. Atmos. Sci.* 76, 561–582.

- Cintineo, J.L., Smith, T.M., Lakshmanan, V., Brooks, H.E., Ortega, K.L., 2012. An objective high-resolution hail climatology of the contiguous United States. *Weather Forecasting* 27, 1235–1248.
- Costa, S., Mezzasalma, P., Levizzani, V., Alberoni, P.P., Nanni, S., 2001. Deep convection over Northern Italy: synoptic and thermodynamic analysis. *Atmos. Res.* 56, 73–88.
- Davis, S.M., LaDue, J.G., 2004. Nonmeteorological factors in warming verification. In: *Preprints, 22nd Conf. on Severe Local Storms*, Hyannis, MA, Amer. Meteor. Soc., P2.7. Available online at: <https://ams.confex.com/ams/pdfpapers/81766.pdf>.
- Dawson, D.T., Xue, M., Milbrandt, J.A., Yau, M., 2010. Comparison of evaporation and cold pool development between single-moment and multimoment bulk microphysics schemes in idealized simulations of tornadic thunderstorms. *Mon. Wea. Rev.* 138, 1152–1171.
- Dawson, D.T., Mansell, E.R., Jung, Y., Wicker, L.J., Kumjian, M.R., Xue, M., 2014. Low-level ZDR signatures in supercell forward flanks: the role of size sorting and melting of hail. *J. Atmos. Sci.* 71, 276–299.
- Dawson, D.T., Xue, M., Milbrandt, J.A., Shapiro, A., 2015. Sensitivity of real-data simulations of the 3 May 1999 Oklahoma City tornadic supercell and associated tornadoes to multimoment microphysics. Part I: storm- and tornado-scale numerical forecasts. *Mon. Wea. Rev.* 143, 2241–2265.
- Grabowski, W.W., Morrison, H., 2016. Untangling microphysical impacts on deep convection applying a novel modeling methodology. Part II: double-moment microphysics. *J. Atmos. Sci.* 73, 3749–3770.
- Grabowski, W.W., Morrison, H., Shima, S.-I., Abade, G.C., Dziekan, P., Pawlowska, H., 2019. Modeling of cloud microphysics: can we do better? *Bull. Am. Meteor. Soc.* 100, 655–672.
- Hong, S.-Y., Dudhia, J., Chen, S.-H., 2004. A revised approach to ice microphysical processes for the bulk parameterization of clouds and precipitation. *Mon. Wea. Rev.* 132, 103–120.
- Hong, S.-Y., Kim, J.-H., Lim, J.-o., Dudhia, J., 2006. The WRF single moment microphysics scheme (WSM). *J. Korean Meteor. Soc.* 42, 129–151.
- Johnson, M., Jung, Y., Milbrandt, J.A., Morrison, H., Xue, M., 2019. Effects of the representation of rimed ice in bulk microphysics schemes on polarimetric signatures. *Mon. Wea. Rev.* 147, 3785–3810.
- Jung, Y., Xue, M., Zhang, G., 2010. Simulations of polarimetric radar signatures of a supercell storm using a two-moment bulk microphysics scheme. *J. Appl. Meteor. Climatol.* 49, 146–163.
- Kessler, E., 1969. On the distribution and continuity of water substance in atmospheric circulations. In: *On the Distribution and Continuity of Water Substance in Atmospheric Circulations*. Springer, pp. 1–84.
- Khain, A., Pokrovsky, A., 2004. Simulation of effects of atmospheric aerosols on deep turbulent convective clouds using a spectral microphysics mixed-phase cumulus cloud model. Part II: Sensitivity study. *J. Atmos. Sci.* 61, 2963–2982.
- Kumjian, M.R., Ryzhkov, A.V., 2012. The impact of size sorting on the polarimetric radar variables. *J. Atmos. Sci.* 69, 2042–2060.
- Labriola, J., Snook, N., Jung, Y., Putnam, B., Xue, M., 2017. Ensemble hail prediction for the storms of 10 May 2010 in South-Central Oklahoma using single- and double-moment microphysical schemes. *Mon. Wea. Rev.* 145, 4911–4936.
- Labriola, J., Snook, N., Jung, Y., Xue, M., 2019a. Explicit ensemble prediction of hail in 19 May 2013 Oklahoma City thunderstorms and analysis of hail growth processes with several multimoment microphysics schemes. *Mon. Wea. Rev.* 147, 1193–1213.
- Labriola, J., Snook, N., Xue, M., Thomas, K.W., 2019b. Forecasting the 8 May 2017 severe hail storm in Denver, Colorado, at a convection-allowing resolution: Understanding rimed ice treatments in multimoment microphysics schemes and their effects on hail size forecasts. *Mon. Wea. Rev.* 147, 3045–3068.
- Lei, H., Guo, J., Chen, D., Yang, J., 2020. Systematic bias in the prediction of warm-rain hydrometeors in the WDM6 microphysics scheme and modifications. *J. Geophys. Res.-Atmos.* 125, e2019JD030756.

- Lim, K.-S.S., Hong, S.-Y., 2010. Development of an effective double-moment cloud microphysics scheme with prognostic cloud condensation nuclei (CCN) for weather and climate models. *Mon. Wea. Rev.* 138, 1587–1612.
- Lin, Y., Colle, B.A., 2011. A new bulk microphysical scheme that includes riming intensity and temperature-dependent ice characteristics. *Mon. Wea. Rev.* 139, 1013–1035.
- Loftus, A., Cotton, W., 2014. A triple-moment hail bulk microphysics scheme. Part II: verification and comparison with two-moment bulk microphysics. *Atmos. Res.* 150, 97–128.
- Loftus, A.M., Cotton, W.R., Carrió, G.G., 2014. A triple-moment hail bulk microphysics scheme. Part I: description and initial evaluation. *Atmos. Res.* 149, 35–57.
- Luo, L., Xue, M., Zhu, K., Zhou, B., 2017. Explicit prediction of hail using multimoment microphysics schemes for a hailstorm of 19 March 2014 in Eastern China. *J. Geophys. Res.-Atmos.* 122, 7560–7581.
- Luo, L., Xue, M., Zhu, K., Zhou, B., 2018. Explicit prediction of hail in a long-lasting multicellular convective system in Eastern China using multimoment microphysics schemes. *J. Atmos. Sci.* 75, 3115–3137.
- Luo, L., Xue, M., Zhu, K., 2020. The initiation and organization of a severe hail-producing mesoscale convective system in East China: a numerical study. *J. Geophys. Res.-Atmos.* 125 e2020JD032606.
- Lynn, B.H., Khain, A.P., Dudhia, J., Rosenfeld, D., Pokrovsky, A., Seifert, A., 2005a. Spectral (bin) microphysics coupled with a mesoscale model (MM5). Part I: model description and first results. *Mon. Wea. Rev.* 133, 44–58.
- Lynn, B.H., Khain, A.P., Dudhia, J., Rosenfeld, D., Pokrovsky, A., Seifert, A., 2005b. Spectral (bin) microphysics coupled with a mesoscale model (MM5). Part II: simulation of a CAPE rain event with a squall line. *Mon. Wea. Rev.* 133, 59–71.
- Mansell, E.R., 2010. On sedimentation and advection in multimoment bulk microphysics. *J. Atmos. Sci.* 67, 3084–3094.
- Mansell, E.R., Ziegler, C.L., Bruning, E.C., 2010. Simulated electrification of a small thunderstorm with two-moment bulk microphysics. *J. Atmos. Sci.* 67, 171–194.
- Milbrandt, J., McTaggart-Cowan, R., 2010. Sedimentation-induced errors in bulk microphysics schemes. *J. Atmos. Sci.* 67, 3931–3948.
- Milbrandt, J., Morrison, H., 2016. Parameterization of cloud microphysics based on the prediction of bulk ice particle properties. Part III: introduction of multiple free categories. *J. Atmos. Sci.* 73, 975–995.
- Milbrandt, J., Yau, M., 2005a. A multimoment bulk microphysics parameterization. Part I: analysis of the role of the spectral shape parameter. *J. Atmos. Sci.* 62, 3051–3064.
- Milbrandt, J., Yau, M., 2005b. A multimoment bulk microphysics parameterization. Part II: a proposed three-moment closure and scheme description. *J. Atmos. Sci.* 62, 3065–3081.
- Milbrandt, J., Yau, M., 2006a. A multimoment bulk microphysics parameterization. Part III: control simulation of a hailstorm. *J. Atmos. Sci.* 63, 3114–3136.
- Milbrandt, J., Yau, M., 2006b. A multimoment bulk microphysics parameterization. Part IV: sensitivity experiments. *J. Atmos. Sci.* 63, 3137–3159.
- Milbrandt, J., Morrison, H., Dawson, D., Paukert, M., 2021. A triple-moment representation of ice in the predicted particle properties (P3) microphysics scheme. *J. Atmos. Sci.* 78, 1–58.
- Morrison, H., Coauthors, 2020. Confronting the challenge of modeling cloud and precipitation microphysics. *J. Adv. Model. Earth Syst.* 12 e2019MS001689.
- Morrison, H., Milbrandt, J., 2015. Parameterization of cloud microphysics based on the prediction of bulk ice particle properties. Part I: scheme description and idealized tests. *J. Atmos. Sci.* 72, 287–311.
- Morrison, H., Pinto, J.O., 2005. Mesoscale modeling of springtime Arctic mixed-phase stratiform clouds using a new two-moment bulk microphysics scheme. *J. Atmos. Sci.* 62, 3683–3704.
- Morrison, H., Thompson, G., Tatarskii, V., 2009. Impact of cloud microphysics on the development of trailing stratiform precipitation in a simulated squall line: Comparison of one- and two-moment schemes. *Mon. Wea. Rev.* 137, 991–1007.
- Naumann, A.K., Seifert, A., 2016. Evolution of the shape of the raindrop size distribution in simulated shallow cumulus. *J. Atmos. Sci.* 73, 2279–2297.
- Pan, Y., Xue, M., Ge, G., 2016. Incorporating diagnosed intercept parameters and the graupel category within the ARPS cloud analysis system for the initialization of double-moment microphysics: testing with a squall line over South China. *Mon. Wea. Rev.* 144, 371–392.
- Paukert, M., Fan, J., Rasch, P.J., Morrison, H., Milbrandt, J., Shpund, J., Khain, A., 2019. Three-moment representation of rain in a bulk microphysics model. *J. Adv. Model. Earth Syst.* 11, 257–277.
- Planche, C., Tridon, F., Banson, S., Thompson, G., Monier, M., Battaglia, A., Wobrock, W., 2019. On the realism of the rain microphysics representation of a squall line in the WRF Model. Part II: sensitivity studies on the rain drop size distributions. *Mon. Wea. Rev.* 147, 2811–2825.
- Putnam, B.J., Xue, M., Jung, Y., Snook, N., Zhang, G., 2014. The analysis and prediction of microphysical states and polarimetric radar variables in a mesoscale convective system using double-moment microphysics, multinet radar data, and the Ensemble Kalman Filter. *Mon. Wea. Rev.* 142, 141–162.
- Putnam, B.J., Xue, M., Jung, Y., Snook, N.A., Zhang, G., 2017. Ensemble probabilistic prediction of a mesoscale convective system and associated polarimetric radar variables using single-moment and double-moment microphysics schemes and EnKF radar data assimilation. *Mon. Wea. Rev.* 145, 2257–2279.
- Riechelmann, T., Noh, Y., Raasch, S., 2012. A new method for large-eddy simulations of clouds with Lagrangian droplets including the effects of turbulent collision. *New J. Phys.* 14, 065008.
- Seifert, A., 2008. On the parameterization of evaporation of raindrops as simulated by a one-dimensional rainshaft model. *J. Atmos. Sci.* 65, 3608–3619.
- Seifert, A., Beheng, K.D., 2006. A two-moment cloud microphysics parameterization for mixed-phase clouds. Part I: model description. *Meteor. Atmos. Phys.* 92, 45–66.
- Snook, N., Jung, Y., Brotzge, J., Putnam, B., Xue, M., 2016. Prediction and ensemble forecast verification of hail in the supercell storms of 20 May 2013. *Wea. Forecast.* 31, 811–825.
- Thompson, G., Field, P.R., Rasmussen, R.M., Hall, W.D., 2008. Explicit forecasts of winter precipitation using an improved bulk microphysics scheme. Part II: implementation of a new snow parameterization. *Mon. Wea. Rev.* 136, 5095–5115.
- vanZanten, M.C., Coauthors, 2011. Controls on precipitation and cloudiness in simulations of trade-wind cumulus as observed during RICO. *J. Adv. Model. Earth Syst.* 3, M06001.
- Wainwright, C.E., Dawson, D.T.II, Xue, M., Zhang, G., 2014. Diagnosing the intercept parameters of the exponential drop size distributions in a single-moment microphysics scheme and impact on supercell storm simulations. *J. Appl. Meteor. Climatol.* 53, 2072–2090.
- Wang, M., Zhao, K., Pan, Y., Xue, M., 2020. Evaluation of simulated drop size distributions and microphysical processes using polarimetric radar observations for landfalling Typhoon Matmo (2014). *J. Geophys. Res.-Atmos.* 125 e2019JD031527.
- Wen, J., Zhao, K., Huang, H., Zhou, B., Yang, Z., Chen, G., Wang, M., Wen, L., Dai, H., Xu, L., Liu, S., Zhang, G., Lee, W.-C., 2017a. Evolution of microphysical structure of a subtropical squall line observed by a polarimetric radar and a disdrometer during OPACC in Eastern China. *J. Geophys. Res.-Atmos.* 122, 8033–8050.
- Wen, L., Zhao, K., Zhang, G., Liu, S., Chen, G., 2017b. Impacts of instrument limitations on estimated raindrop size distribution, radar parameters, and model microphysics during Mei-Yu season in East China. *J. Atmos. Ocean. Tech.* 34, 1021–1037.
- Wen, L., Zhao, K., Wang, M., Zhang, G., 2019. Seasonal variations of observed raindrop size distribution in East China. *Adv. Atmos. Sci.* 36, 346–362.
- Witt, A., Eilts, M.D., Stumpf, G.J., Johnson, J., Mitchell, E.D.W., Thomas, K.W., 1998. An enhanced hail detection algorithm for the WSR-88D. *Wea. Forecast.* 13, 286–303.
- Wyatt, A., Witt, A., 1997. The effect of population density on ground-truth verification of reports used to score a hail detection algorithm. In: *Preprints, 28th Conf. on Radar Meteorology*, Austin, TX, Amer. Meteor. Soc. pp. 368–369.
- Xu, F., Zheng, Y., Xiao, H., Mu, X., 2016. Mesoscale characteristics of a severe hail event over the area along Yangtze River in Jiangsu. *Meteor. Mon. (in Chinese)* 42, 567–577.
- Xu, X., Xue, M., Wang, Y., Huang, H., 2017. Mechanisms of secondary convection within a Mei-Yu frontal mesoscale convective system in Eastern China. *J. Geophys. Res.-Atmos.* 122, 47–64.
- Xue, M., Droegemeier, K., Wong, V., Shapiro, A., Brewster, K., 1995. Advanced Regional Prediction System (ARPS) version 4.0 user's guide. Center for Analysis and Prediction of Storms, University of Oklahoma, p. 380.
- Xue, M., Droegemeier, K.K., Wong, V., 2000. The Advanced Regional Prediction System (ARPS) – a multi-scale nonhydrostatic atmospheric simulation and prediction tool. Part II: model dynamics and verification. *Meteor. Atmos. Phys.* 75, 161–193.
- Xue, M., Droegemeier, K.K., Wong, V., Shapiro, A., Brewster, K., Carr, F., Weber, D., Liu, Y., Wang, D., 2001. The Advanced Regional Prediction System (ARPS) – a multi-scale nonhydrostatic atmospheric simulation and prediction tool. Part II: model physics and applications. *Meteor. Atmos. Phys.* 76, 143–165.
- Xue, M., Wang, D., Gao, J., Brewster, K., Drogemeier, K.K., 2003. The Advanced Regional Prediction System (ARPS), storm-scale numerical weather prediction and data assimilation. *Meteor. Atmos. Phys.* 82, 139–170.
- Xue, L., Fan, J., Lebo, Z.J., Wu, W., Morrison, H., Grabowski, W.W., Chu, X., Geresdi, I., North, K., Stenz, R., Gao, Y., Lou, X., Bansemmer, A., Heymsfield, A.J., McFarquhar, G. M., Rasmussen, R.M., 2017. Idealized simulations of a squall line from the MC3E field campaign applying three bin microphysics schemes: Dynamic and thermodynamic structure. *Mon. Wea. Rev.* 145, 4789–4812.
- Zhang, G., Vivekanandan, J., Brandes, E., 2001. A method for estimating rain rate and drop size distribution from polarimetric radar measurements. *IEEE T. Geosci. Remote.* 39, 830–841.
- Zhang, G., Sun, J., Brandes, E.A., 2006. Improving parameterization of rain microphysics with disdrometer and radar observations. *J. Atmos. Sci.* 63, 1273–1290.
- Zhu, K., Coauthors, 2018. Evaluation of real-time convection-permitting precipitation forecasts in China during the 2013–2014 summer season. *J. Geophys. Res.-Atmos.* 123, 1037–1064.
- Zhu, K., Xue, M., Ouyang, K., Jung, Y., 2020. Assimilating polarimetric radar data with an ensemble Kalman filter: OSSEs with a tornadic supercell storm simulated with a two-moment microphysics scheme. *Q. J. Roy. Meteor. Soc.* 146, 1880–1900.